Two-dimensional flow of foam around a circular obstacle: local measurements of elasticity, plasticity and flow

Benjamin Dollet[1],[*] and François Graner[1]

[1]*Laboratoire de Spectrométrie Physique, BP 87,*

38402 Saint-Martin-d'Hères Cedex, France

Abstract

We investigate the two-dimensional flow of a liquid foam around circular obstacles by measuring all the local fields necessary to describe this flow: velocity, pressure, bubble deformations and rearrangements. We show how our experimental setup, a quasi-2D "liquid pool" system, is adapted to the determination of these fields: the velocity and bubble deformations are easy to measure from 2D movies, and the pressure can be measured by exploiting a specific feature of this system, a 2D effective compressibility. To describe accurately bubble rearrangements, we propose a new, tensorial descriptor. All these quantities are evaluated via an averaging procedure that we justify showing that the fluctuations of the fields are essentially random. The flow is extensively studied in a reference experimental case; the velocity presents an overshoot in the wake of the obstacle, the pressure is maximum at the leading side and minimal at the trailing side. The study of the elastic deformations and of the velocity gradients shows that the transition between plug flow and yielded regions is smooth. Our tensorial description of T1s highlight their correlation both with the bubble deformations and the velocity gradients. A salient feature of the flow, notably on the velocity and T1 repartition, is a marked asymmetry upstream/downstream, signature of the elastic behaviour of the foam. We show that the results do not change qualitatively when various control parameters (flow rate, bubble area, fluid fraction, bulk viscosity, obstacle size and boundary conditions) vary, identifying a robust quasistatic regime. These results are discussed in the frame of the actual foam rheology literature, and we argue that they constitute a severe test for existing rheological models, since they capture both the elastic, plastic and fluid behaviour of the foam.

[*]Electronic address: b.dollet@utwente.nl; Present address: Physics of Fluids, University of Twente, PO Box

217, 7500 AE Enschede, The Netherlands.

I. INTRODUCTION

Liquid foams have a ubiquitous mechanical behavior: depending on the strength of an external applied solicitation, they can exhibit both elastic, plastic or viscous response ([23, 50]). This complex behavior is used in many industrial applications ([28]), like ore flotation, oil extraction, food and cosmetic industry. Liquid foams are also of fundamental interest as models to study complex fluids, since their constitutive item, the bubble, is experimentally easily observable, contrary to colloids or polymers. The understanding of foam rheology has motivated active research; a series of seminal studies has first focused on the elastic properties of foams, such as elastic moduli or yield stress ([15, 27, 40, 46]). The plasticity of foams originates from topological rearrangements, called T1s (Fig. 2c). This coupling between local rearrangements of constitutive entities and a macroscopic plastic behaviour is a general feature of many materials (emulsions, pastes, slurries), that studies have described generically as soft glassy materials ([45]). On the other hand, the research on the viscous and dissipative properties of foams is rather recent ([7, 14, 17, 26]).

Much effort is currently devoted to integrate elastic, plastic and viscous behaviours in a single constitutive equation ([23, 51, Marmottant *et al.*]). To achieve such a goal, a fine and precise knowledge of the mechanical behavior of the foam is required. This is the reason why foams are often studied in quasi-2D geometries ([11, 48]), where foams are confined so that they are only one bubble thick (confinement either between two parallel plates, between one horizontal plate and the surface of a soap solution, or at the free surface of a soap solution). Imaging is easy in these quasi-2D geometries, contrary to an opaque 3D foam. A classical way to study quasi-2D foams consists in using rheometric flows ([32]), like simple shear flows ([13, 33]), which are easy to analyze. The study of heterogeneous flows is complementary: it is less easy to analyze and to understand, but it enlarges the number of observed effects. This is the case for example for flows in constrictions ([1]), or for Stokes experiments, i.e. flows around obstacles ([8, 10, 12, 16, 18, 19]).

We studied extensively Stokes experiments for foams, focusing on the effect of the foam on the obstacle: drag ([16]), lift ([18]) or torque ([19]). The variations of these quantities with various control parameters, especially the foam flow rate, illustrate the interplay between elastic, plastic and viscous behavior of the foam. To go beyond these force and torque measurements, we revisit here some of these experiments with the complementary approach,

studying by local measurements the effect of the presence of an obstacle on a flowing foam. We present a method developed to analyze precisely and completely this local response, quantified by various local fields. We extract velocity and velocity gradients, bubble deformations, and pressure, which describe the elastic and viscous parts of the foam response. We also define a new tensorial descriptor of the bubble rearrangements, and present the corresponding field, which quantifies accurately foam plastic response. The results highlight the differences of the foam local response with respect to simple viscoplastic and viscoelastic responses, namely a marked up/downstream asymmetry, signature of a delayed, elastic response of the foam, and a strong plastic response wherever the bubble deformation becomes close to a critical, yield strain. Our results thus call for a modelisation coupling elastic, plastic and fluid behavior, and they also constitute an extensive database to test and constrain such models.

II. MATERIALS AND METHODS

A. Experiment

We perform a Stokes experiment ([1, 10, 12, 16]), i.e. we study the flow of foam around obstacles (Fig. 1), using a foam channel fully described in [16]. Briefly, a tank is filled with a bulk solution obtained by adding 1% of commercial dish-washing liquid (Taci, Henkel) to desionised water. Its surface tension, measured with the oscillating bubble method, is $\gamma = 26.1 \pm 0.2$ mN m^{-1}, and its kinematic viscosity, measured with a capillary viscosimeter, is 1.06 ± 0.04 mm s^{-2} unless explicitly stated. Nitrogen is blown in the solution through a nozzle or a tube at a computer controlled flow rate. This generates a "liquid pool foam" foam [48], constituted by a horizontal monolayer of monodisperse bubbles (dispersity < 3%) of average thickness h_0, confined between the bulk solution and a glass top plate. This is a quasi-2D foam ([11, 48]): despite the 3D geometry of the bubbles (Fig. 1b), it experiences 2D horizontal flows, which minimizes the effect of drainage. Two others quasi-2D foams exist: the bubble raft (no confinement), and the Hele-Shaw cell (confinement between two horizontal plates). Contrary to these two systems, the liquid pool foam has an effective in-plane compressibility ([16]), which enables to measure pressure easily, as recalled in Section II C 1. The fluid fraction is adjusted by the foam thickness [42]; its value is 7%. The foam

flows around an obstacle placed at the middle of the channel; in the present study, we choose the flow rate between 24 and 515 ml min^{-1} (corresponding velocities: 0.11 to 2.5 cm s^{-1}). In this paper, we will study a reference case characterized by the following values of the parameters: circular obstacle of diameter 30 mm, flow rate of 176 ml min^{-1}, bubble area of 16.0 mm^2, foam thickness of 3.5 mm, and bulk viscosity of 1.06 mm^2 s^{-1}. We will then study the influence of each control parameter separately.

This setup has allowed us to measure forces on obstacles ([16, 18]) and pressure drops associated to the flow of foam ([17]). For the purpose of the present paper, we record for every experiment a stack of 750 images, representing a movie of 30 seconds. From these movies, we extract all relevant quantities describing the flow of foams: velocity, pressure, elastic stress, bubble deformations, and bubble swapping (topological rearrangements, or T1s) using a home-made procedure, as follows.

B. Image analysis

1. Skeletonisation of experimental images

With the NIH Image software, we invert the grey levels of the images, then threshold our images, to clearly separate the black network of edges from white bubbles. We have defined several zones on the image each with different thresholds, to compensate from slight remaining spatial variations of light intensity. We finally extract the network of the bubble edges from the experimental images by a classical skeletonisation procedure, which reduces the foam to a network of one-pixel thick edges (Fig. 2a).

This procedure conserves the topology between the real and the skeletonized bubbles (Figs. 1a and 2a), which enables a proper evaluation of the bubble deformation, as explained in Section II C 3. It has two limitations: first, it distorts the geometry and curvature of the bubbles edges and vertices, which prevents us from evaluating precisely the elastic stress, since this requires integration along all edges ([3]). Second, it is not adapted to the boundaries; we therefore systematically eliminate the data near the obstacle and the channel walls.
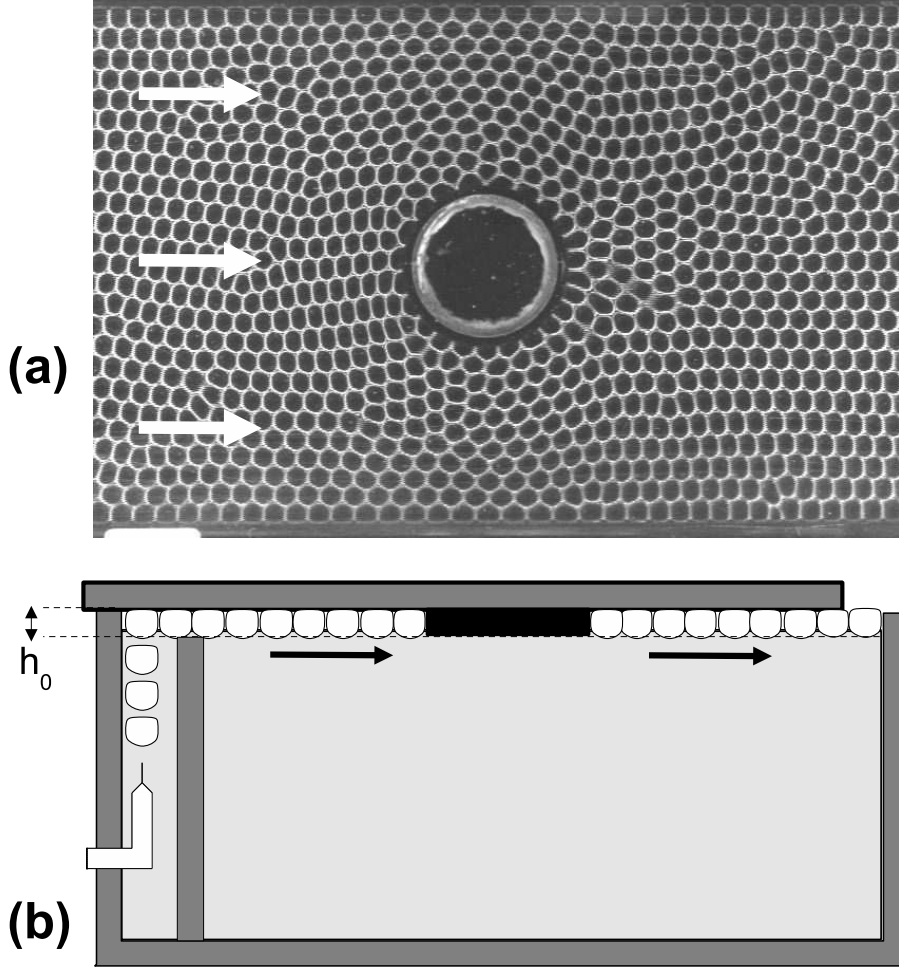
FIG. 1: (a) Photo of foam flowing from left to right (arrows) around a circular obstacle of diameter 30 mm. The bubble size is 16.0 mm^2 (note the monodispersity of the foam), and the flow rate is 176 ml min^{-1}. The walls of the channel (width 10 cm) are visible at the top and bottom of the picture. The surface of the observed field is 15.4×10.2 cm^2. Movies are available at `http://www-lsp.ujf-grenoble.fr/recherche/a3t2/a3t2a1/mousses2d3d.htm`. (b) Side view of the setup. The foam is constituted by a monolayer of bubbles and the black rectangle represents the obstacle.

2. *Treatment of skeletonized images*

For a 2D skeletonized foam, the bubbles are bounded by thin edges, which merge in threefold vertices. Bubbles are thus easily labelized, and a vertex can be unambiguously defined as a black pixel for which, among its eight neighboring pixels, one can find three
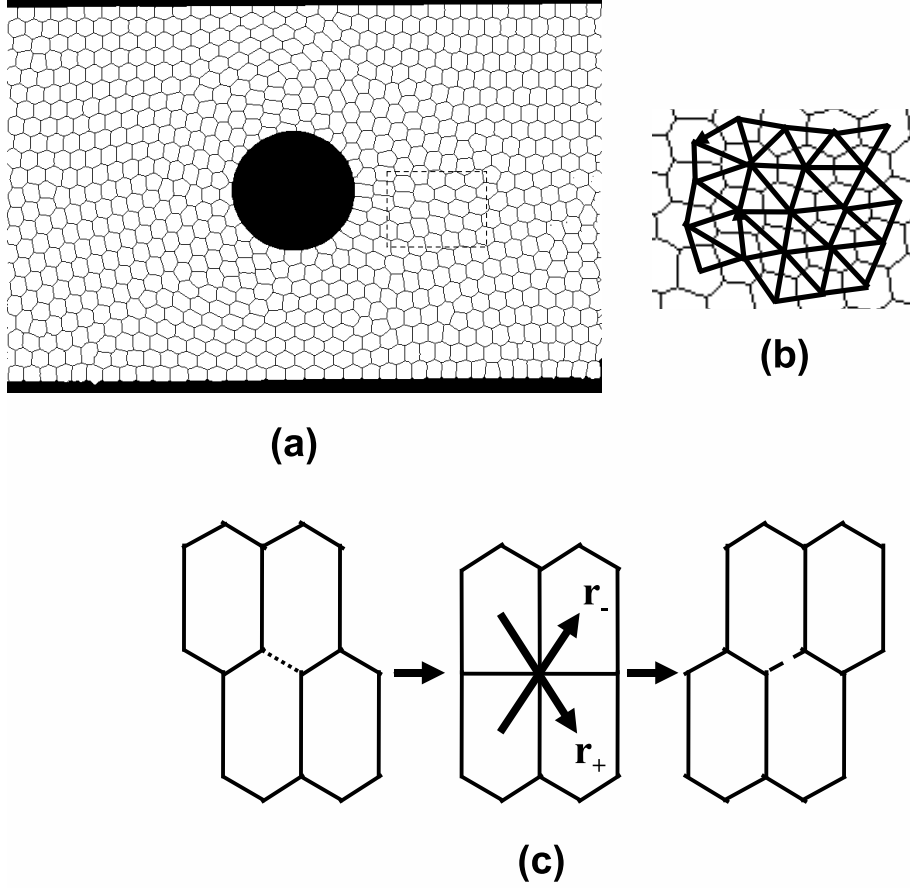
FIG. 2: (a) Skeletonized image of foam. (b) Zoom on the zone framed in (a): the network of bubble edges is figured with thin lines, and the (triangular) center network with thick lines. (c) Sketch of a side swapping (topological rearrangements, also called T1 event). Left: the edge to disappear is dotted; middle: definition of the vectors $\vec{r}_+$ and $\vec{r}_-$; right: the new edge is dashed.

pixels belonging to three different bubbles. Boundaries vertices are defined as pixels on boundaries, with two neighboring pixels belonging to two different bubbles.

We scan an image in two steps. In a first step, each individual bubble is labelized with a different number. The program records a list of bubbles, each bubble being represented by its number b, its number of pixels N_b, and the position $\vec{x}_b$ of its barycenter. In a second step, vertices are identified and labelized, and the program records them in a second list, each vertex being represented by its number, its coordinates and the label of its neighboring bubbles. The subsequent analysis does not require the image.

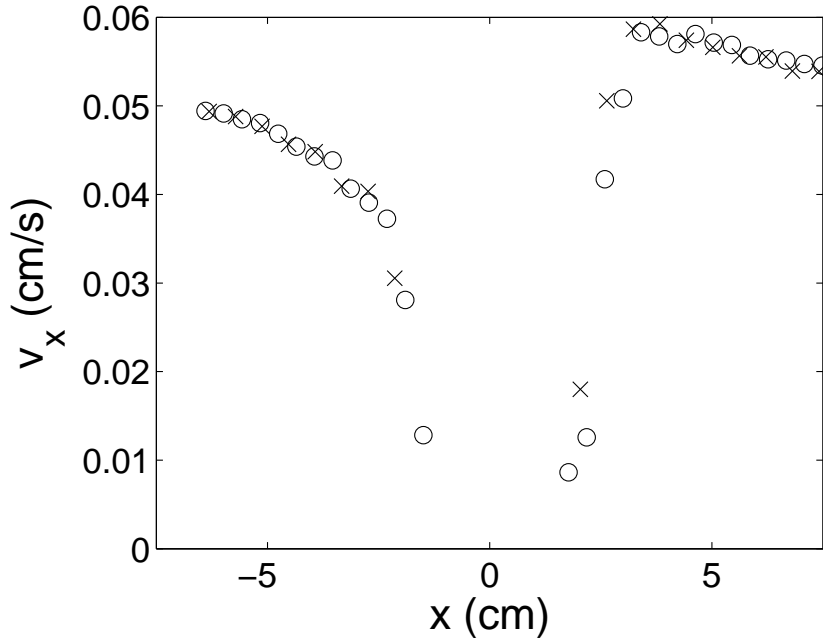To compute the fields, we mesh the image by a rectangular grid. We have checked that

FIG. 3: Plot of the velocity v_x along the axis of symmetry of the flow, as a function of the streamwise coordinate x, for a flow rate of 24 ml min^{-1} and for two mesh sizes ($\times$: boxes of area 6.0×6.2 mm^2, $\circ$: boxes of area 4.1×4.1 mm^2).

there exists a mesh size for which the results do not change (Fig. 3): this validates our choice, and is a first indication of the continuous character of the foam (see section III A). We have chosen to mesh the image with a rectangular grid of 26×17 (nearly) square boxes of side 6 mm: such a choice enables us to capture well the variations at the macroscopic scale, and the statistics is sufficient for these variations to be smooth (during the whole movie, about 2×10^3 bubbles are computed per box). For simplicity, each bubble is attributed to the box where its center lies even if part of it belongs to other boxes.

3. Direct measurements from skeletonized images

From the list of bubbles, we compute the network of the vectors $\vec{r}$ linking two centers of bubbles in contact, which we call the center network (Fig. 2b). To be precise, each vector $\vec{r}$ is attributed to the two boxes (with a coefficient $1/2$ each) of the two bubble centers it

binds. We then compute the texture tensor ([2]):

$$\bar{\bar{M}} = \langle \vec{r} \otimes \vec{r} \rangle, \tag{1}$$

which is the second-order tensor of components: $M_{ij} = \langle r_i r_j \rangle$. The average is performed over 750 images and all vectors in the box. This tensorial quantity has proven to be a good descriptor of bubble deformation: it reproduces the size, direction and amplitude of deformation of bubbles, in studies where it has been computed over the bubble edges network $\vec{\ell}$ ([1, 9, 24]). Here, we calculate it over the center network. With such a choice, the texture tensor definition (1) is much more general than with the bubble edges network: it applies to 3D foams, and to wet foams such as the ones considered hereby. It is also more robust, because the center of masses, hence the vectors $\vec{r}$, is much less biased by skeletonisation than the bubble edges. Anyway, the two possible network choices are equivalent at low bubble deformation.

In order to compute the velocity field, we compare successive frames. In the studied range of flow rates, the displacement of a bubble between two successive frames is small compared to its size; the displacement of the bubble centers is thus easy to calculate, and we average all displacements on each box to get the velocity field (Eulerian rather than Lagrangian point of view).

The calculation of the T1s is also based on the correlation of two successive images; a T1 is a topological neighbor-swapping event, during which a bubble edge disappears and a new one is created (Fig. 2c). The program tracks independently the disappearing and appearing edges, by comparing the list of edges of two successive frames. This decoupling of the disappearing and appearing edges is necessary for two reasons: first, the duration of a T1 event may be longer than the time interval between two successive frames (0.04 s); second, the transient fourfold vertex (middle of Fig. 2c) contains a certain amount of liquid. After skeletonisation, this is often erroneously recognized as an artificial little four-sided bubble between the four bubbles experiencing the T1, which we have to remove by imposing a lower threshold on the bubble area. Actually, a T1 covers two distinct instantaneous events: one disappearance and one apparition of a link between two bubbles. To a disappearing (appearing) edge is associated the vector of the center network $\vec{r}_-$ ($\vec{r}_+$) which links the centers of the two separating (attaching) bubbles. A complete quantification of T1s, including not only their frequency but also their direction, must rely on these vectors, whose

9

direction is irrelevant by definition. We thus define the tensors $\bar{\bar{T}}_\pm = f_\pm \langle \vec{r}_\pm \otimes \vec{r}_\pm \rangle$, where f_+ (f_-) is the frequency of separation (attachment) events per link $\vec{r}$ of the center network ([Marmottant et al.]). Preliminary studies show that these tensors are closely related to the mechanical properties of the foam ([Marmottant et al.]). However, in this paper, we use a more intuitive definition, based on unit vectors: $\bar{\bar{T}}_\pm^{\text{adim}} = f_\pm \langle \hat{r}_\pm \otimes \hat{r}_\pm \rangle$, because it has the advantage to be directly proportional to the frequency of T1s.

C. Computation of the fields

We present here the relevant fields describing the flow of foams, and the way they are computed from the image analysis detailed in the previous section.

1. Pressure

As already mentioned in a previous study ([16]), in a quasi-2D setup with foam confined between a top plate and a liquid pool, the depth of bubbles adjust to pressure variations. The 3D compressibility of the bubbles is negligible here: for an ideal, isothermal gas, the compression modulus is of order 10^5 Pa, which is 4 orders of magnitude higher to the measured local variations of pressure, as shown later (Fig. 11). Hence, the volume of a given bubble is constant; but if its pressure increases, its depth increases to maintain equilibrium with the hydrostatic pressure of the bulk solution, hence its visible area decreases: the foam has an effective 2D compressibility in the plane of the top plate. The precise relationship between bubble area and pressure is established in another paper ([42]), in which we show that the relative uncertainty in pressure equals 2%. It writes:

$$P - P_0(x) = \frac{\rho g \mathcal{V}}{A} + 2\gamma \sqrt{\frac{\pi}{A}}, \tag{2}$$

with $\rho = 10^3$ kg m^{-3} the volumetric mass of the solution, $g = 9.8$ m s^{-2} the gravity acceleration, and $\mathcal{V}$ the constant bubble volume. Here, P_0 is the local reference pressure, which embodies the constant pressure gradient along the channel ([17]): hence, $P - P_0$ is the local variation of pressure due to the presence of the obstacle. The average bubble area is easily computed in each box with the image analysis program. Since the pressure field is scalar, it is convenient to represent it in gray levels.

2. Velocity and velocity gradients

The image analysis program provides directly the velocity field, which we represent as usual with arrows. The velocity gradient is computed by finite differences; we evaluate this gradient in the middle of the four boxes (i, j), $(i, j + 1)$, $(i + 1, j)$ and $(i + 1, j + 1)$. We rather use the symmetric velocity gradient, the deformation rate: $\bar{\bar{D}} = (\overline{\overline{\nabla v}} + {}^t\overline{\overline{\nabla v}})/2$, and the antisymmetric velocity gradient, the vorticity, which is a scalar for 2D flows: $\omega = \frac{1}{2}\left(\frac{\partial v_y}{\partial x} - \frac{\partial v_x}{\partial y}\right)$. We will precise the graphical representation of the deformation rate, and of the others tensorial quantities, in the following sections. We will also use the scalar dissipation function ([22]), defined as: $\|\bar{\bar{D}}\| = \sqrt{D_{xx}^2 + 2D_{xy}^2 + D_{yy}^2}$.

3. Tensorial fields: texture, statistical elastic strain, T1

As stated in Section II B 2, we use the texture tensor as a descriptor of bubble deformations. To be more quantitative, we will use the statistical elastic strain tensor, defined as ([2]):

$$\bar{\bar{U}} = \frac{1}{2}(\ln \bar{\bar{M}} - \ln \bar{\bar{M}}_0), \tag{3}$$

where $\bar{\bar{M}}_0$ is a reference value, that we choose isotropic: $\bar{\bar{M}}_0 = \lambda_0 \bar{\bar{I}}$. Here, λ_0 is the average of the eigenvalues of the texture tensors evaluated at the upstream and downstream extremities of the observation field (left and right on Fig. 1), where the bubbles are less perturbed by the presence of the obstacle, and $\bar{\bar{I}}$ is the 2D identity tensor. We use the statistical elastic strain tensor because it quantifies the elastic strain in foams, extending the classical elastic strain ([30]) to plastic flows. The trace of this tensor quantifies the relative variation of area of the bubbles, which remains lower than 10% ([16]); hence, in general, this tensor will have a positive eigenvalue and a negative one. We choose to represent such a tensor by two orthogonal lines, as explained in Fig. 4a. The positive (negative) eigenvector represent the direction and amplitude of traction (compression) of deformed bubbles compared to the reference state. We also use this representation for the deformation rate which, like the statistical elastic strain, is an almost traceless tensor, since the flow remains weakly compressible. Here, the positive (negative) eigenvector represent the direction and amplitude of maximal elongation (compression) rate.

Finally, we represent the T1s by the two tensors $\bar{\bar{T}}_+^{\mathrm{adim}}$ and $\bar{\bar{T}}_-^{\mathrm{adim}}$ (Section II B 2); these
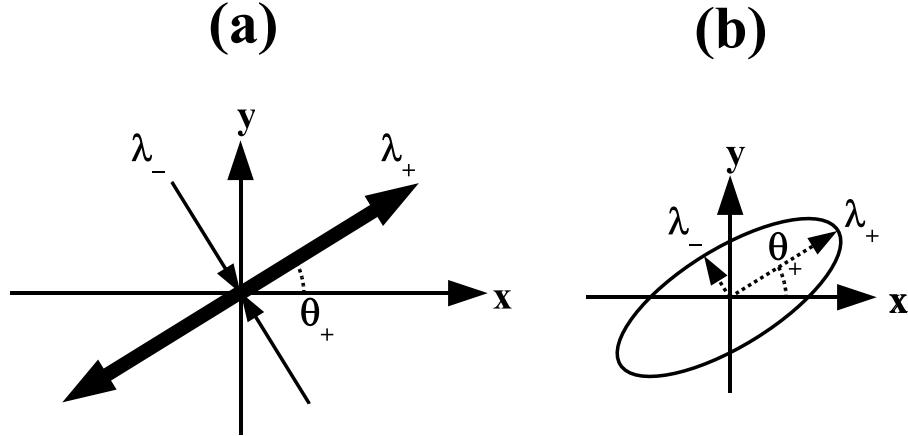
(a) **(b)**

FIG. 4: Representation of symmetric tensors (i.e. with orthogonal eigenvectors): (a) representation of a tensor with two eigenvalues of different sign ($\lambda_- < 0 < \lambda_+$). The thick (thin) line represents the direction and magnitude of the positive (negative) eigenvalue; (b) elliptic representation of a tensor with strictly positive eigenvalues ($0 < \lambda_- < \lambda_+$).

two tensors are symmetric with strictly positive eigenvalues; there is therefore suitably represented by ellipses (Fig. 4b) of parameterized equations:

$$
\begin{pmatrix} x_\pm(t) \\ y(_\pm t) \end{pmatrix} = \bar{\bar{T}}_\pm^{\mathrm{adim}} \cdot \begin{pmatrix} \cos t \\ \sin t \end{pmatrix} = \begin{pmatrix} (T_\pm^{\mathrm{adim}})_{xx} \cos t + (T_\pm^{\mathrm{adim}})_{xy} \sin t \\ (T_\pm^{\mathrm{adim}})_{xy} \cos t + (T_\pm^{\mathrm{adim}})_{yy} \sin t \end{pmatrix}.
$$

In this case, the major axis is the preferred direction for T1s to occur. We justify this (new) way to quantify T1s in Section III B 5.

III. RESULTS

In this section, we present the local measurements for a foam flowing around an obstacle. We first focus on a reference case: the flow of a monodisperse foam (bubble area: 16.0 mm^2, foam thickness: 3.5 mm, bulk viscosity: 1.06 mm^2 s^{-1}, flow rate: 176 ml min^{-1}) around a circular obstacle of diameter 30 mm. We compare averages and fluctuations of a local field to show that the foam behaves like a continuous medium (section III A). We then present a full study of the reference case (section III B), and separate the influence of each control parameter (section III C).

A. Averages *versus* fluctuations

Can we consider the foam as a continuous medium in our case? This is not obvious *a priori*, since the steady flow arises from a balance between the load experienced by the bubbles passing around the obstacle, and the discrete relaxations occurring during T1 events ([31]): locally-defined quantities like elastic stress or statistical elastic strain fluctuate around an average value. We consider here the influence of such fluctuations and their correlations, since various studies have shown their great importance, especially when T1 avalanches occur ([13, 25]), leading to strong stress drops ([33, 39]).

To address this question, we analyse the temporal fluctuations of a local quantity for our reference case, in the same spirit as ([24]). We have chosen the statistical elastic strain tensor $\bar{\bar{U}}$, but the analysis would be similar on other local quantities such as velocity or pressure. More precisely, we have chosen to analyse one scalar quantity extracted from $\bar{\bar{U}}$: the square of the difference between the two eigenvalues $[\lambda_+(\bar{\bar{U}}) - \lambda_-(\bar{\bar{U}})]^2$. This quantity scales as the elastic energy associated to shear strain; hence, it is expected to exhibit some huge drops if T1 avalanches occur, since they release a lot of elastic energy. We have analysed the fluctuations in a box close to the trailing side of the obstacle (Fig. 5a, right), where fluctuations are expected to be strong; we will see later that this is also a region where T1s are frequent. The temporal variations of the bubble deformation is reported in Fig. 5a. Qualitatively, we do not observe a behavior dominated by T1 avalanches: such a behavior would correspond to a succession of low increases (load) and quick drops (relaxation) of the elastic energy. Quantitatively, we analyse the increments of the bubble deformation between two successive images, and report the histogram of the distribution of these increments in Fig. 6a. This histogram is well fitted by a Gaussian curve, characteristic of a white noise, and we do not observe an asymmetric distribution with a lot of small increases and a number of large decreases, which would correspond to T1 avalanches.

However, the considered box is a small box, where only seven bubbles in average are present at a given instant. One could thus argue that fluctuations are dominated by advection, not by possible T1 avalanches occurring at larger scale. We thus analyse the fluctuations at a larger scale, choosing a box 18 times bigger, in the wake of the obstacle (Fig. 5b, right). The relative fluctuations are much smaller (Fig. 5b), and the increments are here again well fitted by a Gaussian curve (Fig. 6b).
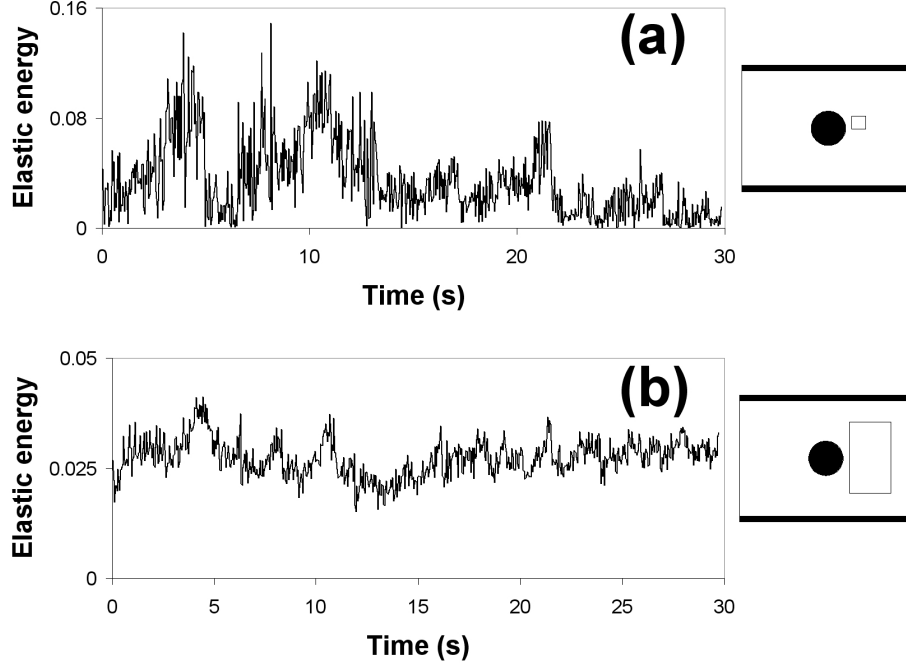
FIG. 5: Temporal evolution of the quantity $[\lambda_+(\bar{\bar{U}}) - \lambda_-(\bar{\bar{U}})]^2$, which scales as the elastic energy. (a) Results on a box of size 1.2×1.1 cm^2 (sketched at the right side). (b) Results on a box of size 3.6×6.2 cm^2.

We have performed this quantitative analysis of the fluctuations only in our reference experiment, but we observed in the other experiments analysed here that the fluctuations do not present large-scale correlations; they are similar to a random, white noise and play a negligible role at large scales. We will thus only focus on coarse-grained average quantities, and treat the foam as a continuous medium. The generality of such an approach is discussed in Section IV A.

B. Study of a reference case

For each studied field, we proceed as follows: we first present a map of the whole field, and we then study the variation of the field components along various lines: two directed streamwise, one on the axis of the obstacle and another aside, at 2.5 cm from the axis of symmetry of the flow; and three directed spanwise: one passing through the center of the obstacle, one upstream and the symmetric downstream one, both lines being at 2.4 cm from the middle axis (Fig. 7).
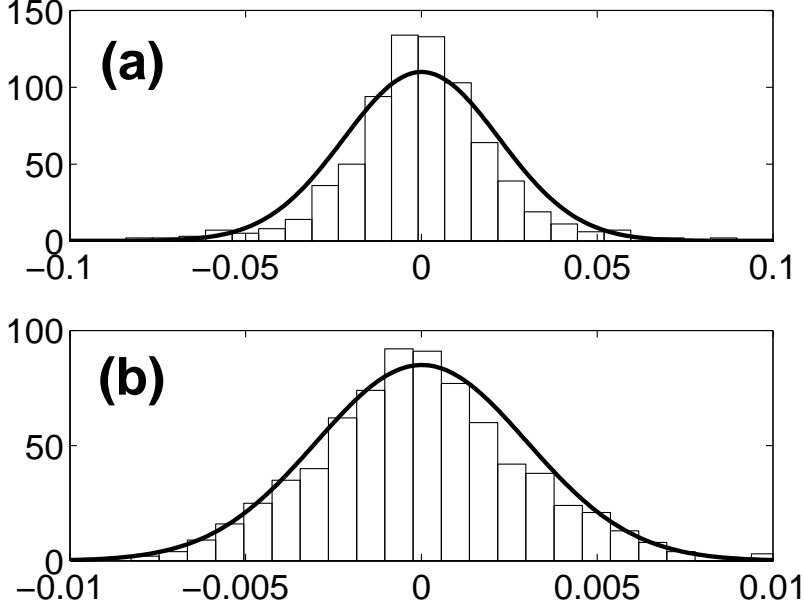
FIG. 6: Histogram of the increments of the the quantity $[\lambda_+(\bar{\bar{U}}) - \lambda_-(\bar{\bar{U}})]^2$. (a) Results on a box of size 1.2×1.1 cm^2 (average: 3.7×10^{-5}, standard deviation: 2.2×10^{-2}). (b) Results on a box of size 3.6×6.2 cm^2 (average: -8.4×10^{-6}, standard deviation: 3.0×10^{-3}). The curves superimposed are Gaussian curves with the same mean and standard deviation as the increments.

1. Velocity

The whole velocity field is presented in Fig. 8. Qualitatively, the flow far from the obstacle is a plug flow, as already observed for foam flows in narrow channels ([6]). The obstacle imposes two symmetric stagnation points, one upstream and one downstream, and the flow is constricted, thus accelerated, on the sides of the obstacle.

To study quantitatively the velocity, we divide it by the averaged velocity v_0 obtained from the upstream and downstream extremities of the observation region, where the flow is less perturbed: v_0 is therefore the velocity of the plug flow. We report the two components of $(\vec{v} - \vec{v}_0)/v_0$, which is the dimensionless velocity deviation from the plug flow, in Fig. 9. This figure shows a striking feature: the velocity is asymmetric up/downstream. More precisely, on the axis $y = 0$, the component v_x shows an overshoot upstream, whereas it decreases monotonically downstream. The asymmetry is also obvious for the comparison of v_x between the axis $x = -2.4$ and 2.4 cm: the perturbation from the plug flow is higher
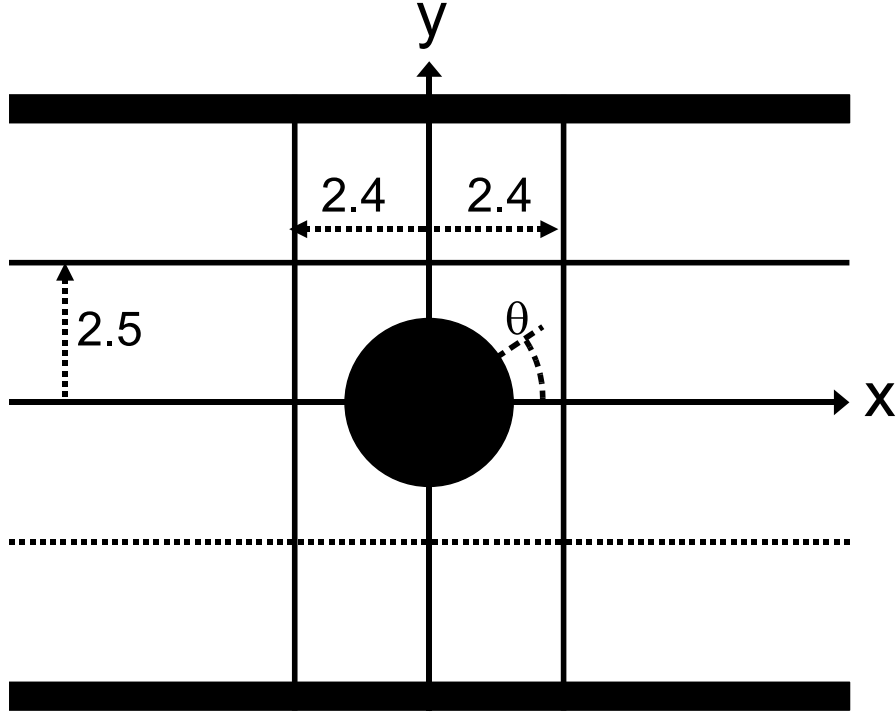
FIG. 7: Sketch of the lines where the fields are evaluated. The streamwise direction is x, the spanwise is y. We choose five lines: the axis of symmetry of the flow, $y = 0$, an axis at the side of the obstacle, $|y| = 2.5$ cm (the dashed axis means that there are two such symmetric axes; the evaluated quantities will be averaged on these both axes). Three axis are perpendicular to the flow direction: $x = -2.4$, 0 and 2.4 cm.

upstream than downstream for v_x, but lower for v_y. As expected, the v_y component vanishes on the $y = 0$ axis.

2. Pressure

The whole pressure field is presented in Fig. 10. The pressure is maximal at the leading side of the obstacle, and is minimal at its trailing side. We can also note that the increase of pressure upstream is very progressive, extending farther than the limits of the observation field. Fig. 11 displays the evolution of the pressure along the five axes of Fig. 7. We also observe an asymmetry up/downstream; contrary to the velocity, this asymmetry is more obvious on the side of the obstacle than on the axis $y = 0$: the pressure perturbation changes
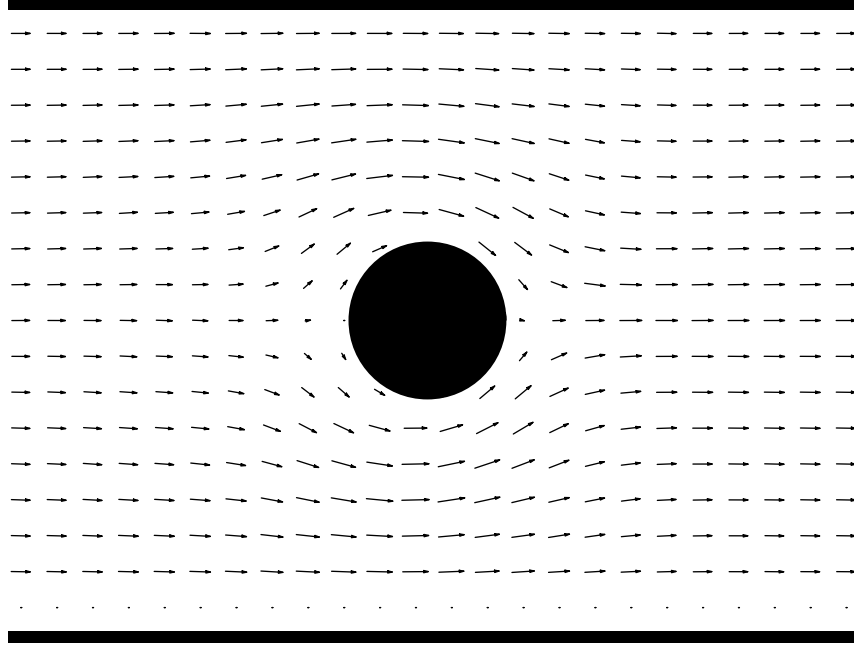
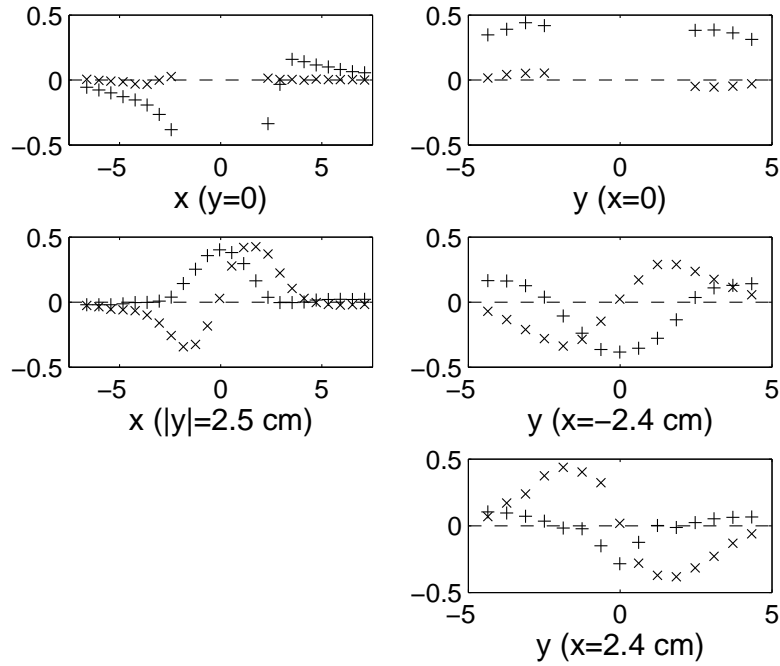FIG. 8: Velocity field around a circular obstacle.

FIG. 9: Velocity components around a circular obstacle: $(v_x - v_0)/v_0$ (+), and v_y/v_0 (×). The length unity is the centimeter.
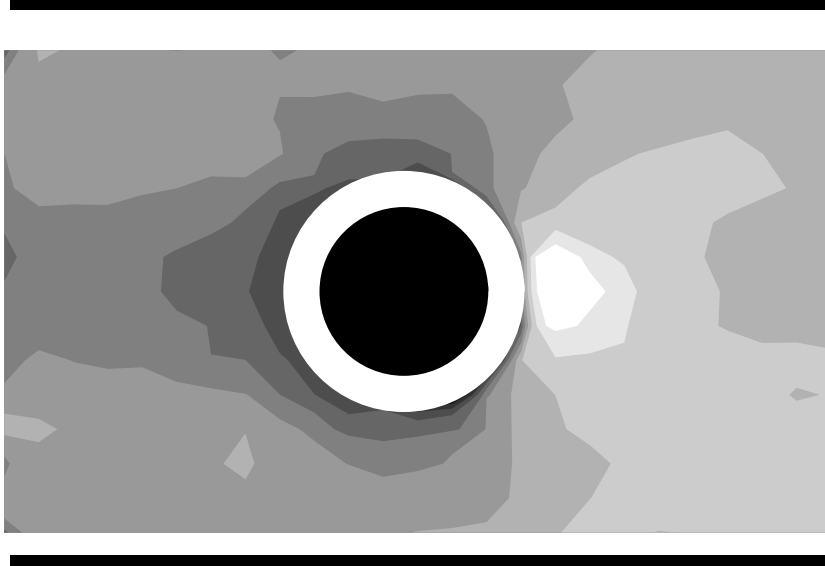
FIG. 10: Pressure field around a circular obstacle. The higher the pressure, the darker the gray level. The difference between two successive gray levels is 1.5 Pa, corresponding to a relative variation in area of 2.5%. The white circle around the obstacle is the region where the bubble area, hence the pressure, cannot be reliably evaluated.

sign at $y = 2$ cm. Note also that along the axis $x = 0$, the decrease of the perturbation in pressure with the distance to the obstacle is quicker than the perturbation in velocity.

3. Statistical elastic strain

We now study the statistical elastic strain field, defined by Eq. (3), to quantify the bubble deformation, as explained in Section II C 3. We display this field in Fig. 12 using the representation explained in Fig. 4b. We note that the deformation is not negligible for the bubbles entering the observation field: they are slightly stretched in the spanwise direction. The bubbles are stretched in the x direction on the sides and in the wake of the obstacle, and in the y direction at the leading side of the obstacle and on the sides of the wake.

The statistical elastic strain field $\bar{\bar{U}}$ is a symmetric tensor, hence it has three indepen-dent components U_{xx}, U_{xy} and U_{yy}. Instead of these three components, we have chosen to represent the combinations $U_{xx} + U_{yy}$, $U_{xx} - U_{yy}$ and U_{xy}. The trace $U_{xx} + U_{yy}$ gives access to the dilatation, whereas the difference $U_{xx} - U_{yy}$ compares the bubble deformation in the
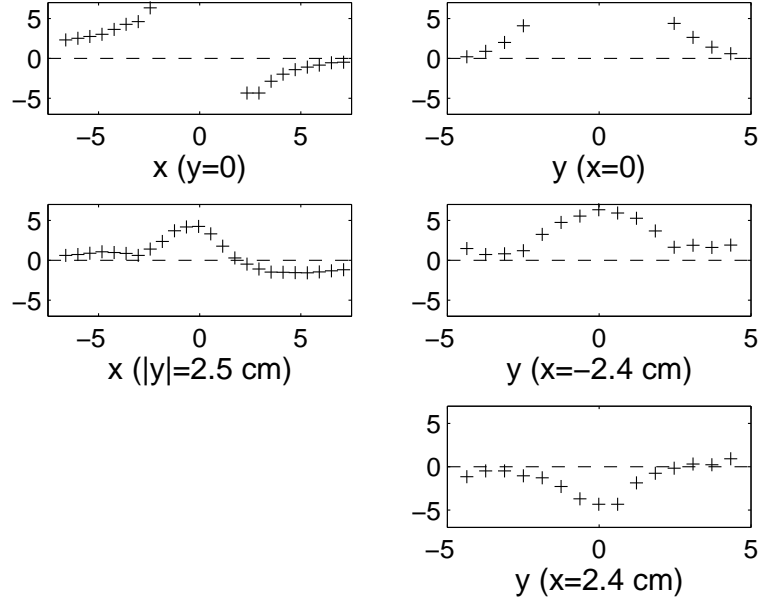
18

FIG. 11: Pressure evolution (in Pa) around a circular obstacle. The pressure is obtained from the bubble area from Eq. (2); more precisely, we report here the difference between the local pressure an
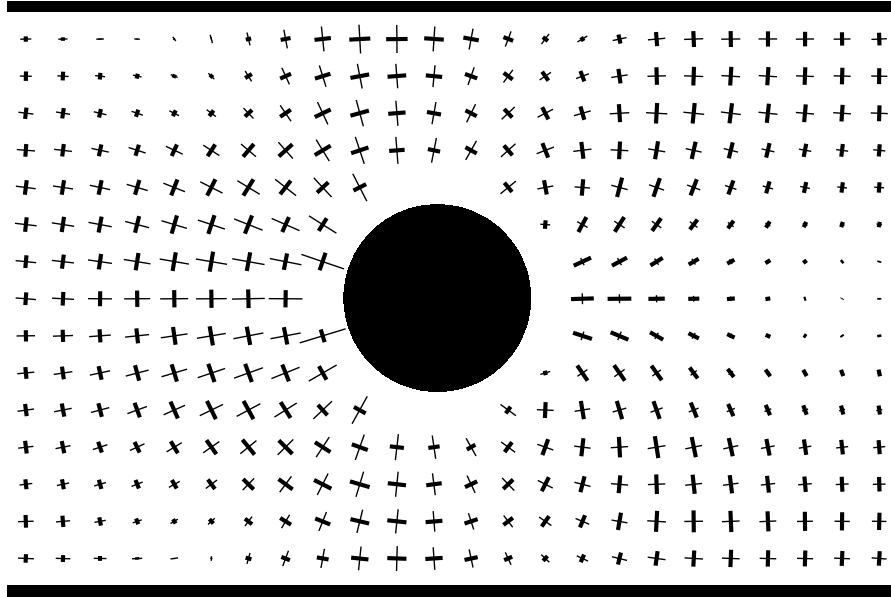

FIG. 12: Statistical elastic strain field around a circular obstacle. The thick (thin) line is a direction of maximal elongation (compression), see Fig. 4a.

19

directions parallel and perpendicular to the flow, and the U_{xy} component indicates the deviation of the deformation from the x and y directions. These combinations are plotted in Fig. 13 along the five axis of Fig. 7. First, the trace has a weak amplitude (its absolute value remains lower than 0.1), and its evolution is strongly anti-correlated to the pressure (Fig. 11). The explanation of such a trend is easy: when the pressure increases, the bubble area decreases as explained in Section II C 1. Hence, the length of the vectors $\vec{r}$ linking centers of neighboring bubbles decreases, and so does $U_{xx} + U_{yy} \approx \ln r/r_0$ after Eq. (3). Second, we consider the parameter $U_{xx} - U_{yy}$. It tends towards a negative value far from the obstacle, which confirms the spanwise stretch observed on Fig. 12. This trend is observed both upstream and downstream, hence we think that it is due to the longitudinal pressure gradient due to the pressure drop along the channel. More interestingly, the presence of the obstacle strongly modifies the deformation of the bubbles: considering the downstream axis ($x = 2.4$ cm), the bubbles are stretched streamwise in the wake, and spanwise on the sides on the wake, the transition occurring at $|y| = 1.5$ cm. On the other hand, on the upstream axis ($x = -2.4$ cm) the bubbles are stretched spanwise close to the symmetry axis of the flow, and streamwise on the sides, the transition occurring at $|y| = 2$ cm. Third, the U_{xy} component on the sides of the obstacle ($|y| = 2.5$ cm) changes sign at two different points ($x = 0$ and 2 cm), showing that the orientation of the maximal deformation rotates of about $180°$ during the passage around the obstacle. Note also that this component is not strictly reversed between upstream and downstream (comparison of the axis $x = -2.4$ and $y = 2.4$ cm).

4. Velocity gradients

We now turn to the velocity gradients. We first show the map of the deformation rate in Fig. 14. It confirms that the 2D effective compressibility of the flow (see Section II C 1) remains weak, because the absolute values maximal elongation and the maximal compression are very close at any point. Furthermore, the amplitude of the deformation rate decreases quickly with the distance to the obstacle, and seems to become negligible upstream and downstream for a distance comparable with the obstacle diameter. To investigate whether this amplitude really vanishes at a finite distance from the obstacle, as expected for a Bingham plastic in the same flow conditions ([37]), we consider the (scalar) dissipation
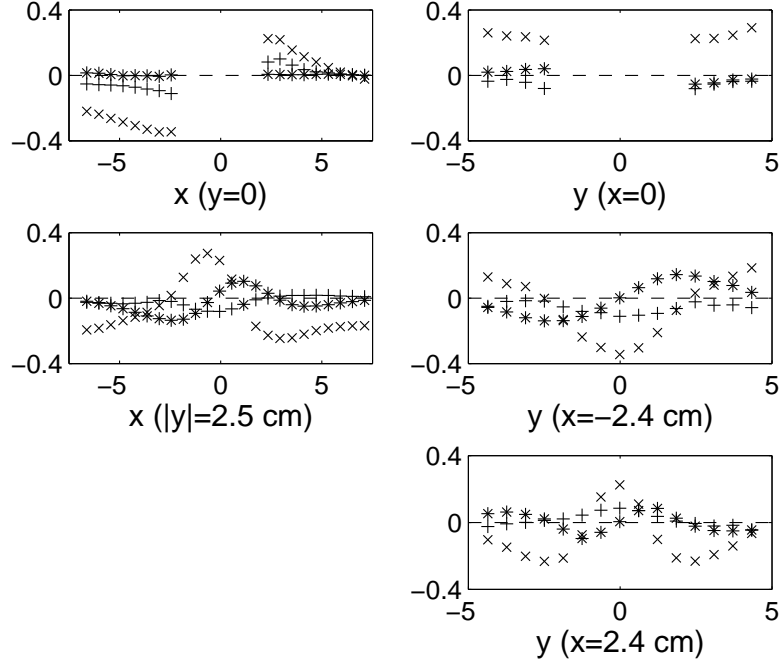
FIG. 13: Combinations $U_{xx} + U_{yy}$ (+), $U_{xx} - U_{yy}$ (×) and U_{xy} (∗) of the statistical elastic strain field around a circular obstacle.

function (see Section II C 3), and plot its logarithm along the two symmetry axis $x = 0$ and $y = 0$ (Fig. 15). This plot reveals that the dissipation function decreases with the distance of the obstacle, but does not vanish. It is possible that it vanishes indeed farther from the obstacle, but we have not investigated this possibility further. Furthermore, the decrease is more complex than a power-law or exponential decrease, and is quicker downstream than upstream.

The map of the vorticity is presented in Fig. 16. The vorticity exhibits significant variations, antisymmetric with respect to the $y = 0$ axis: in the $y > 0$ half-channel, it is negative on the side of the obstacle, and positive downstream (there is also a little positive zone just before the obstacle). The asymmetry up/downstream is once more obvious, as well as the wake.
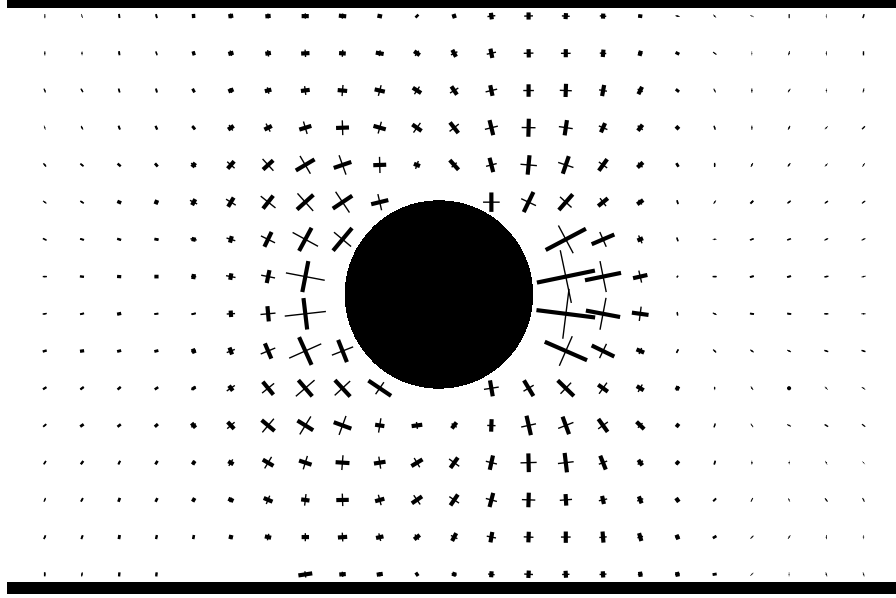
21

FIG. 14: Deformation rate field around a circular obstacle. The thick (thin) line represents the maximal elongation (compression) rate, see Fig. 4a.
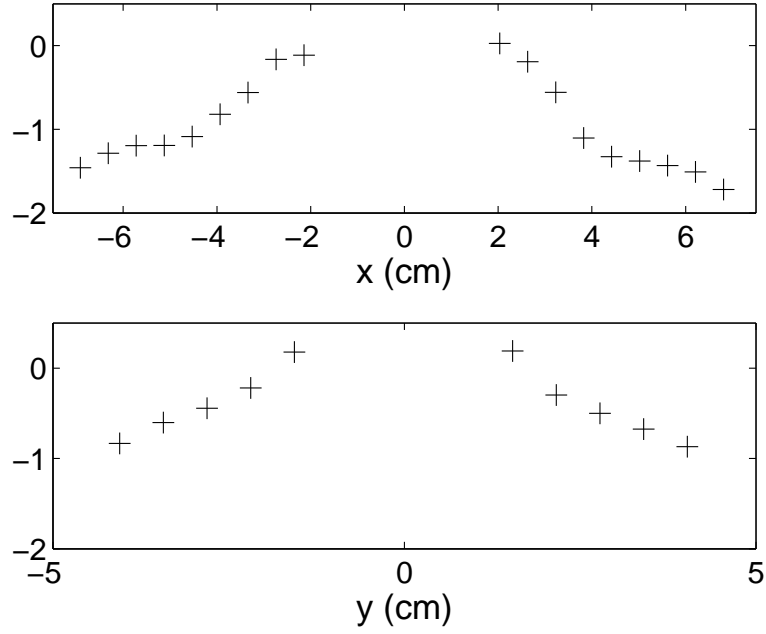

FIG. 15: Logarithm of the dissipation function (expressed in s^{-1}) as a function of x on the $y = 0$ axis (top), and as a function of y on the $x = 0$ axis (bottom).
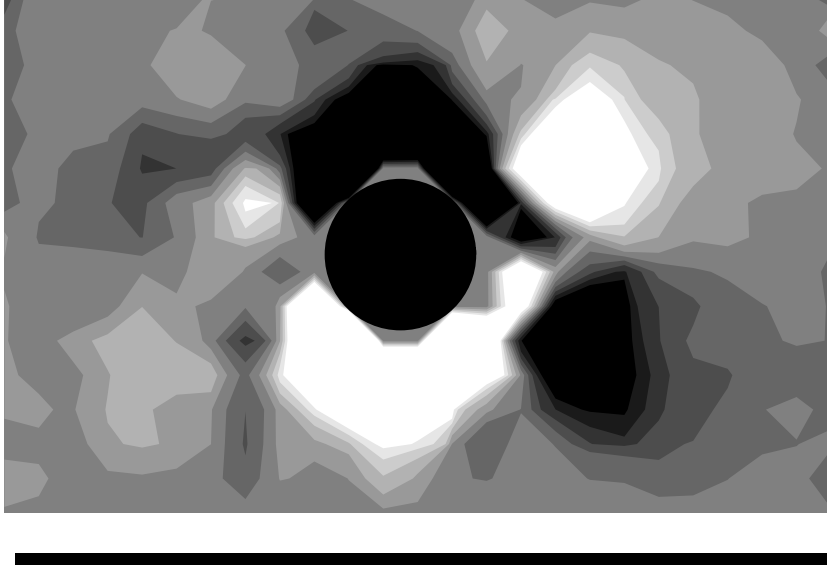
FIG. 16: Vorticity field around a circular obstacle. The light (dark) grey levels represent positive (negative) vorticity.

5. T1 quantification

We first investigate the validity of our measurements of T1s. As explained in Section II B 2, the calculation of appearing and disappearing edges is decoupled; therefore, we have to check whether the number of these two kinds of events is the same, as should be if we record correctly the T1s. Furthermore, we have emphasized that our method may be sensitive to artifacts. We have calculated the following quantity:

$$\sum_{\text{every box } i} |f_+ - f_-|_i \bigg/ \sum_{\text{every box } i} (f_+ + f_-)_i = 7.0\%,$$

which quantifies the relative uncertainty of our method, acceptable despite the various sources of errors.

We now represent the map of T1s in Fig. 17, which illustrates the advantages of the tensorial representation: not only does it contain the number of T1s (proportional to the size of the ellipses, as discussed in Section II B 2), but also their direction. The major axes of the two kinds of ellipses are mainly orthogonal, which illustrates the fact that plastic events release high stresses in one direction to the perpendicular direction ([38]). Quantitatively,
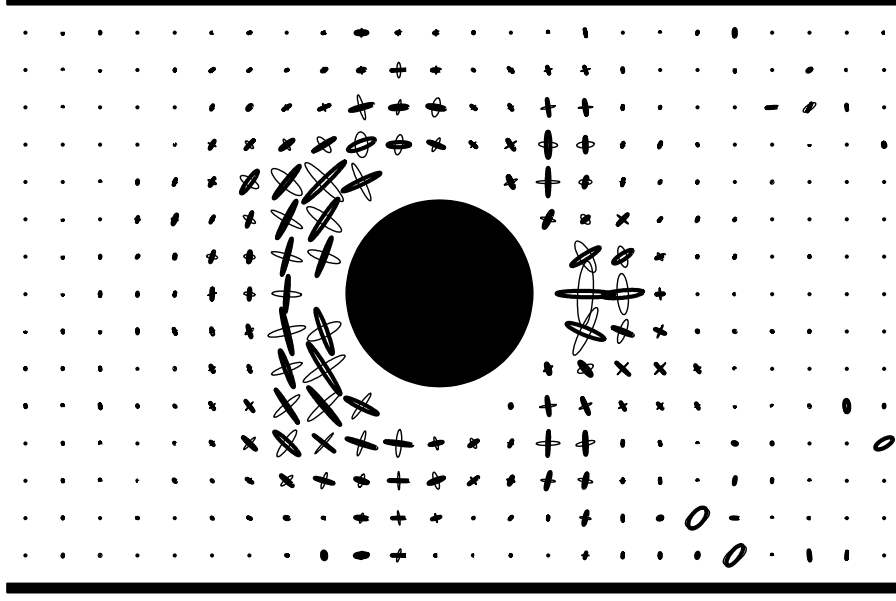
23

FIG. 17: Elliptical representation of T1s: the thick (thin) ellipses represent the tensor $\bar{\bar{T}}^{\mathrm{adim}}_{+}$ ($\bar{\bar{T}}^{\mathrm{adim}}_{-}$), defined in Section II B 2. The preferential direction of the T1s is obvious in the adopted tensorial representation. Note the few remaining artifacts (bottom right).

denoting $\vec{x}_{+}$ ($\vec{x}_{+}$) the unit vector of the major axis of the ellipse representing $\bar{\bar{T}}^{\mathrm{adim}}_{+}$ ($\bar{\bar{T}}^{\mathrm{adim}}_{-}$), we calculate for each box the scalar product $\vec{x}_{+} \cdot \vec{x}_{-}$, and report the histogram of this quantity in Fig. 18. This histogram is actually strongly peaked around 0, confirming that $\vec{x}_{+}$ and $\vec{x}_{-}$ are orthogonal. We also calculate the average and standard deviation of the scalar product $\vec{x}_{+} \cdot \vec{x}_{-}$, weighted by the number of T1s for each box: $\langle \vec{x}_{+} \cdot \vec{x}_{-} \rangle = 7.6 \times 10^{-5}$ and $\delta(\vec{x}_{+} \cdot \vec{x}_{-}) = 1.4 \times 10^{-2} \ll 1$, which proves the orthogonality of appearing and disappearing edges.

Fig. 17 shows that T1s are concentrated close to the obstacle, but again with a significant asymmetry: upstream, the T1s are more distributed and spread widely on the sides on the obstacle, whereas downstream they are more localised in the wake. Note also that the direction of T1s is correlated to the ones of the statistical elastic strain (Fig. 12) and of the deformation rate (fig. 14); such a correlation is probably important to understand better the rheology of foams.

To focus more on the spatial distribution of the frequency of T1s, we now plot $\|\bar{\bar{T}}^{\mathrm{adim}}_{+} - \bar{\bar{T}}^{\mathrm{adim}}_{-}\|/\sqrt{2} = \sqrt{[(T^{\mathrm{adim}}_{+xx} - T^{\mathrm{adim}}_{-xx})^2 + 2(T^{\mathrm{adim}}_{+xy} - T^{\mathrm{adim}}_{-xy})^2 + (T^{\mathrm{adim}}_{+yy} - T^{\mathrm{adim}}_{-yy})^2]/2}$. When
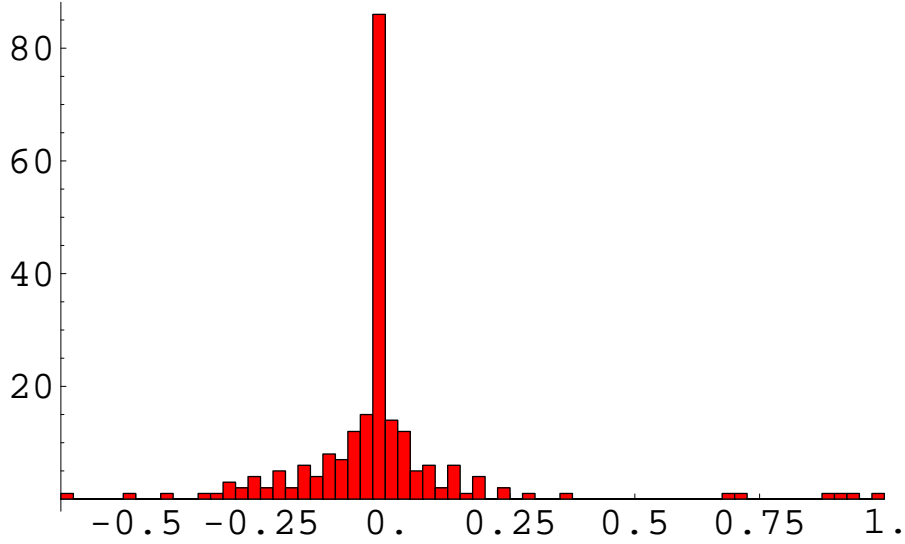
FIG. 18: Repartition histogram of the quantity $\vec{x}_+ \cdot \vec{x}_-$ (see text for definition).

$\vec{x}_+ \cdot \vec{x}_- = 0$, which is in good approximation true, this quantity equals $(f_+ + f_-)/2$; we thus identify it to the frequency of T1s. This quantity has the advantage to reduce strongly the remaining artifacts; its map is presented on Fig. 19. This map shows that the frequency of T1 presents three maxima: one centered in the wake, and two symmetrically off-centered downstream, at an angular position $|\theta| \simeq 3\pi/4$ (see Fig. 7 for the definition of θ). The complex angular dependence of the T1 frequency is illustrated on Fig. 20. It shows that the off-centered downstream maximum arises for an angle $\theta = 145°$, and that frequency of T1s is almost equal for this maximum and for the one located in the wake. Fig. 20 shows also a secondary maximum for $\theta = 55°$.

C. Influence of various control parameters

In this section, we systematically study the dependence of the fields describing the flow of foams around obstacles in the same spirit as in [16]: starting from the reference experiment extensively studied in the previous section, we vary only one control parameter, successively the flow rate (Section III C 1), the bubble area (Section III C 2), the foam thickness (Section III C 3) and the bulk viscosity (Section III C 4). To simplify the discussion, we only study the evolution of three scalar quantities: the velocity component v_x, the pressure P and the quantity $U_{xx} - U_{yy}$, along the axis of symmetry $y = 0$. We end this section by discussing
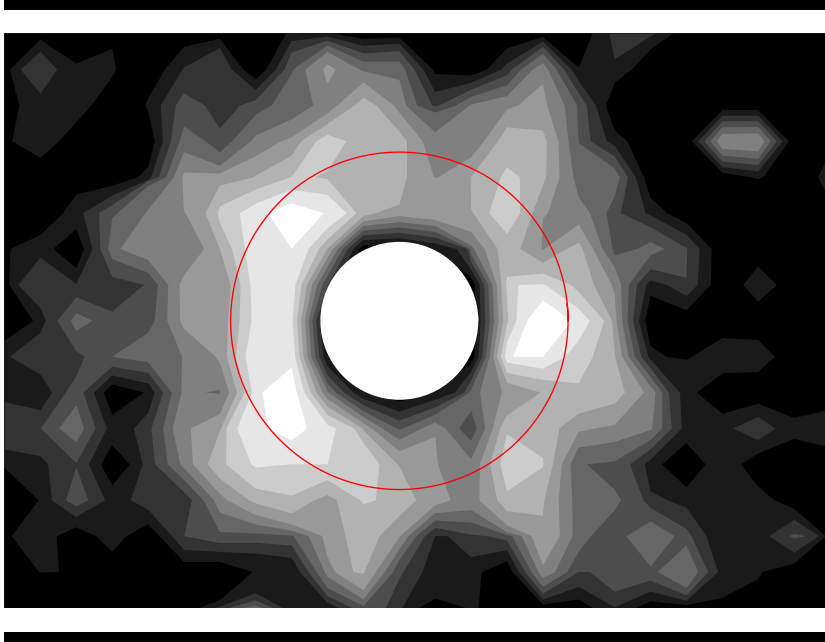
FIG. 19: Spatial distribution of the frequency of T1s. The brighter the grey lever, the higher the frequency of T1s. Note the attenuation of the artifacts in comparison with the Fig. 17, as well as the marked asymmetry up/downstream. The circle indicates the position chosen for the evaluation of Fig. 20.

the influence of the size and shape of the obstacle (Section III C 5).

1. Flow rate

At given bubble area (16.0 mm^2), foam thickness (3.5 mm) and bulk viscosity (1.06 mm^2 s^{-1}), we study five different flow rates: 24, 54, 176, 293 and 515 ml min^{-1} (corresponding velocities v_0: 0.11, 0.26, 0.84, 1.40 and 2.45 cm s^{-1}). To compare more easily the velocities, we consider the dimensionless velocity v_x/v_0. We plot this quantity, as well as the pressure and the component $U_{xx} - U_{yy}$, along the axis $y = 0$, in Fig. 21. Remarkably, all data points collapse on the same master curve for the velocity, the pressure and the bubble deformation, which proves that the qualitative features emphasized in Section III B do not change on the studied range of flow rate.
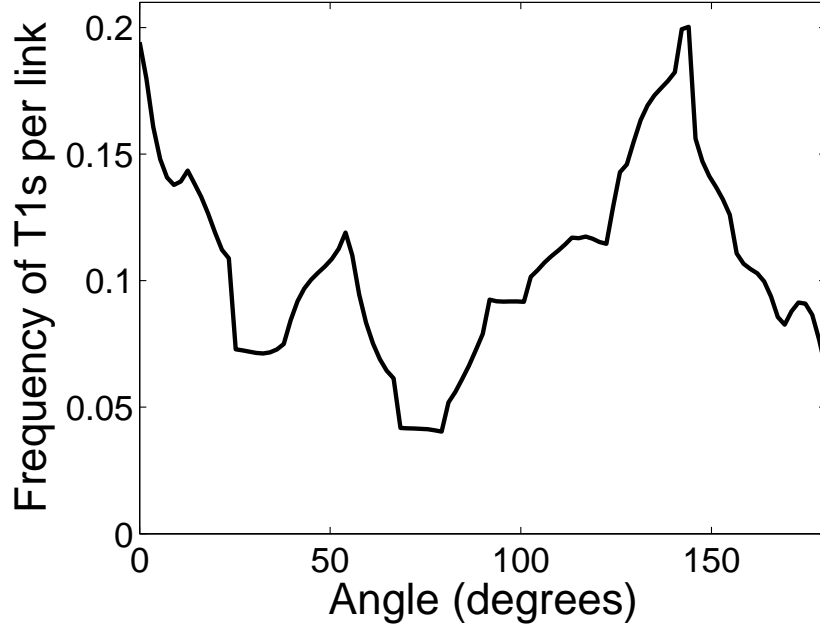
FIG. 20: Angular dependence (in degrees) of the frequency of T1s per unit link, evaluated at 1.5 cm from the boundary of the obstacle. The flow being symmetric with respect to the axis $y = 0$, the data have been averaged with the angles between -180 and $0°$.

2. Bubble area

To study the influence of bubble area, the flow rate cannot be strictly imposed, since it is slaved to target values of the other control parameters. However, as shown in Section III C 1, it has no significant influence on the results. We study for each bubble area: 12.1, 16.0, 20.0, 25.7, 31.7 and 39.3 mm^2, a flow rate as close as possible to the one of the reference case, respectively 160, 176, 166, 133, 150 and 169 ml min^{-1}. The results are reported in Fig. 22. They show that neither the velocity field nor the bubble deformation depends qualitatively on the bubble area. Only the pressure behavior in the wake changes: for big enough bubbles, the pressure release at the trailing side observed in Fig. 11 arises farther, and can be preceded by a compression zone close to the obstacle.
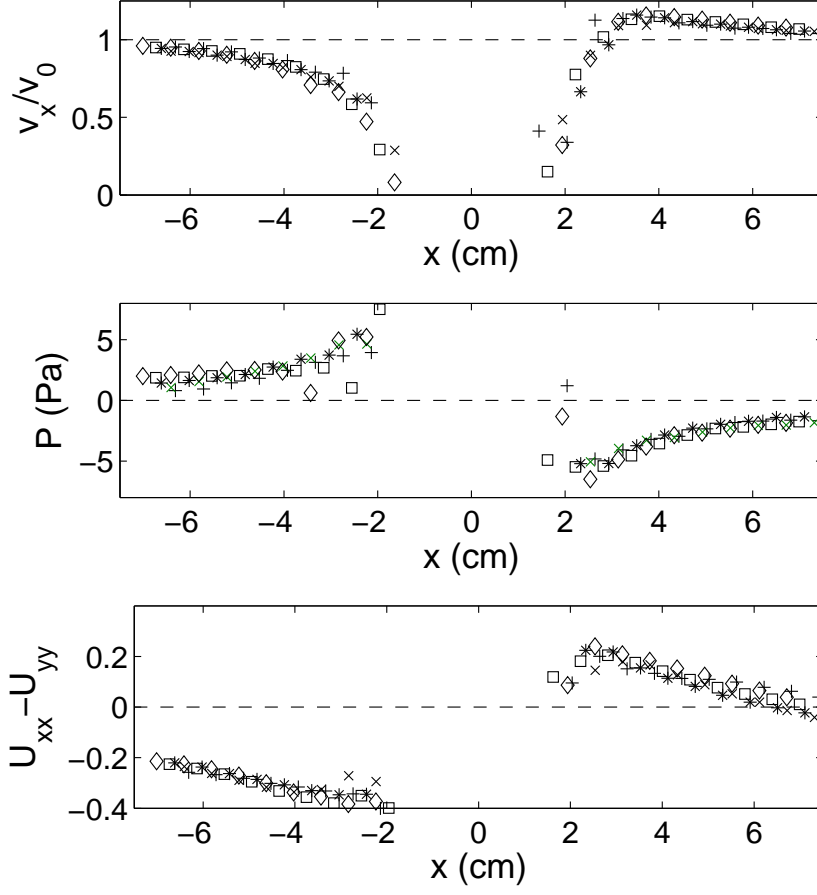
FIG. 21: From top to bottom: plot of the dimensionless velocity v_x/v_0, of the pressure, and of the component $U_{xx} - U_{yy}$, as a function of x along the axis $y = 0$, for the flow rates of 24 (+), 54 (×), 176 (∗), 293 (□) and 515 ml min^{-1} (◇).

3. Foam thickness

Various theoretical ([27, 40]) and experimental ([35, 36, 41, 44]) studies have shown that the fluid fraction plays a crucial role in the foam rheology, but its influence on the local behavior of the foam has so far not been studied in detail. In our case, the foam thickness is a way to change the fluid fraction of the foam: the thicker, the drier the foam. We study six different foam thicknesses: 2.0, 2.5, 3.0, 3.5, 4.0 and 4.5 mm, at fixed bubble area 16.0 mm^2. The corresponding fluid fractions are 8.5, 7.7, 7.4, 6.7, 6.4 and 5.8% (see [42] for the evaluation of these fluid fractions). Since the cross section of the foam varies proportionally
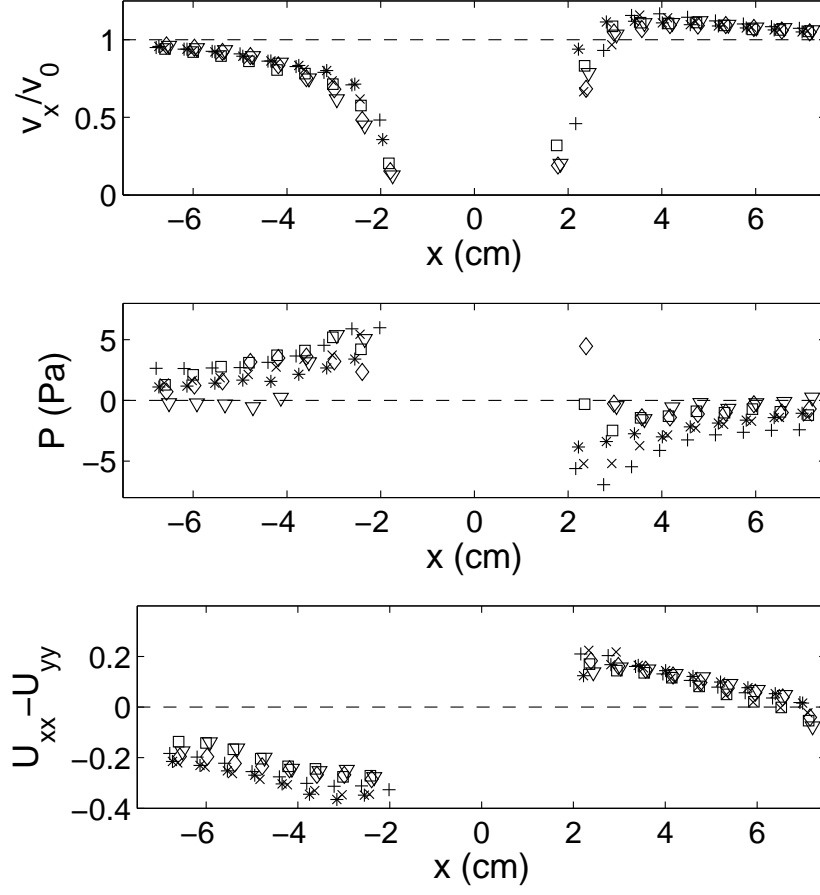
28

FIG. 22: From top to bottom: plot of the dimensionless velocity v_x/v_0, of the pressure, and of the component $U_{xx} - U_{yy}$, as a function of x along the axis $y = 0$, for the bubble area of 12.1 $(+)$, 16.0 $(\times)$, 20.0 $(*)$, 25.7 $(\square)$, 31.7 $(\diamond)$ and 39.3 mm^2 $(\triangledown)$.

to its thickness, we choose a mean velocity v_0 (see Section III B 1) the closest possible to the one of the reference case, respectively 0.67, 0.88, 0.89, 0.84, 0.74 and 0.56 cm s^{-1} for the six thicknesses. Velocity, pressure and bubble deformation are plotted in Fig. 23. We observe the following variations for the lowest foam thicknesses (or highest fluid fractions): the asymmetry in the velocity is weaker, there appears a compression zone in the wake close to the obstacle (like for the biggest bubbles studied in Section III C 2), and the amplitude of the bubble deformation decreases. Note that there is no significant variations for the three highest thicknesses.
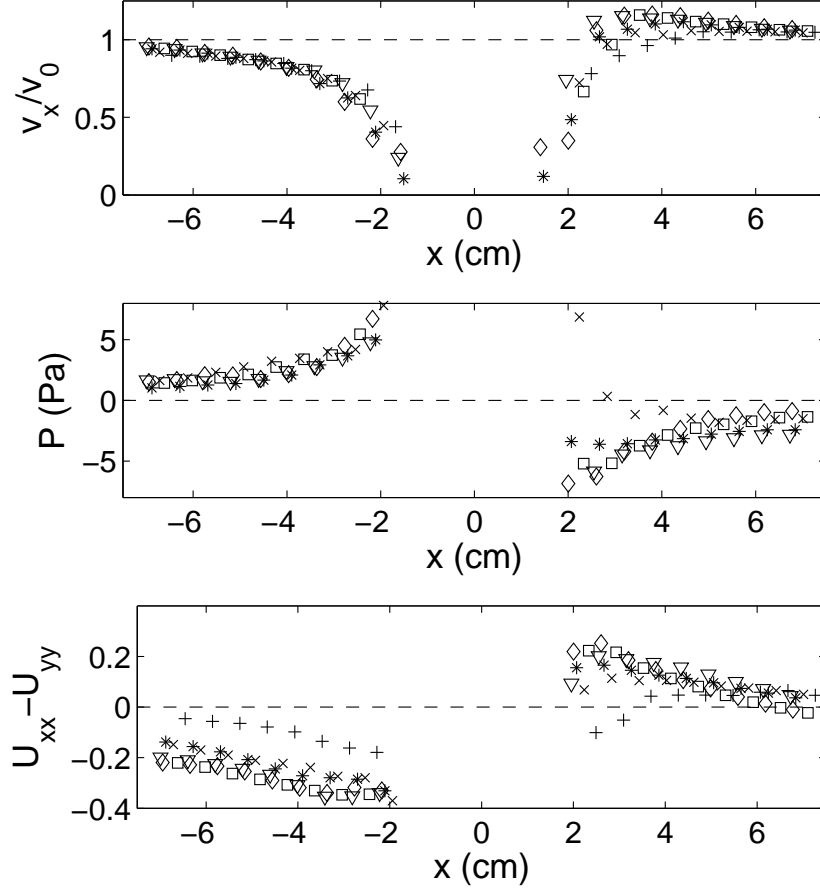
FIG. 23: From top to bottom: plot of the dimensionless velocity v_x/v_0, of the pressure, and of the component $U_{xx} - U_{yy}$, as a function of x along the axis $y = 0$, for the foam thickness of 2.0 (+), 2.5 ($\times$), 3.0 ($*$), 3.5 ($\square$), 4.0 ($\diamond$) and 4.5 cm (∇). Since the bubbles are decompacted, the pressure cannot be calculated for the foam thickness of 2.0 mm.

4. Bulk viscosity

We investigate now the influence of bulk viscosity. From the various cases studied in [16], we only consider the two extremes ones: a soap solution without added glycerol (viscosity: 1.06 mm^2 s^{-1}), and another one with 50% added glycerol in mass (viscosity: 9.3 mm^2 s^{-1}). The bubble area is 20.0 mm^2. The flow rates are 166 and 154 ml min^{-1} for the low and high viscosity cases. The results are presented on Fig. 24. They show that the bulk viscosity has no significant effect, except in the wake close to the obstacle.
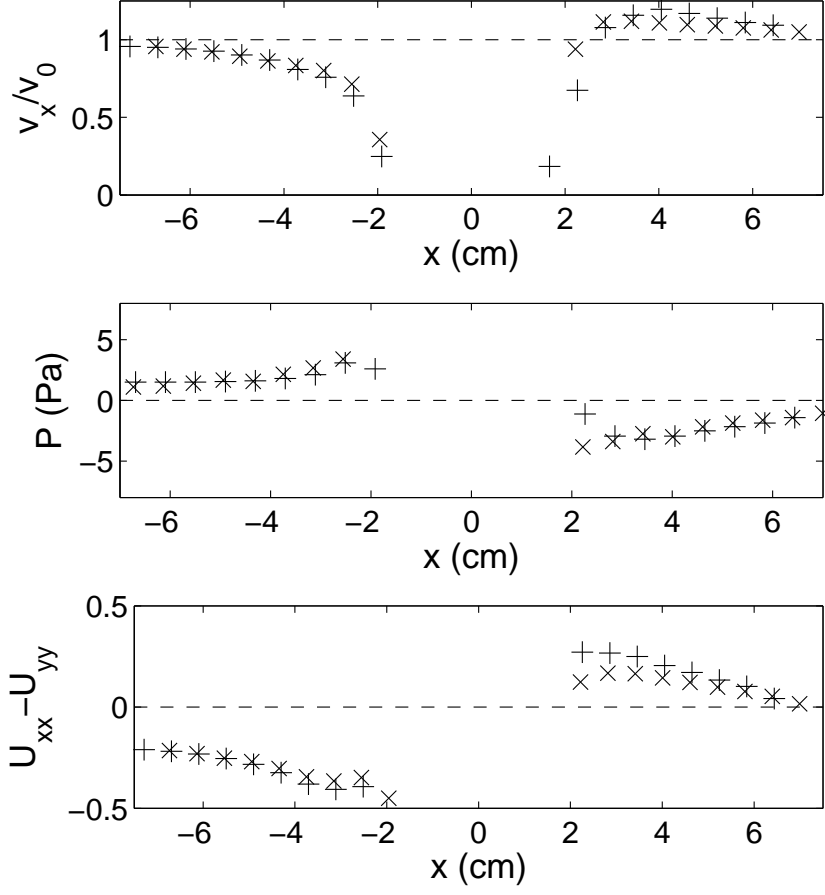
30

FIG. 24: From top to bottom: plot of the dimensionless velocity v_x/v_0, of the pressure, and of the component $U_{xx} - U_{yy}$, as a function of x along the axis $y = 0$, for a bulk viscosity of 1.06 ($\times$), and 9.3 mm^2 s^{-1} ($+$).

To summarize this study of the influence of the following control parameters: flow rate, bubble area, foam thickness and bulk viscosity, we emphasize that the main trends shown in a reference case (Section III B) are robust, especially the up/downstream asymmetry.

5. Obstacle

The last control parameter that we have studied is the obstacle itself. We have shown in previous studies that tuning the obstacle geometry allows to show a variety of behaviors: streamlining for a symmetric airfoil profile ([16]) and anti-inertial lift for a cambered one

31

([18]), and combination of drag, lift and torque for an elliptical obstacle ([19]). Here, we focus on simpler, circular shapes, and compare the reference obstacle, the circle of diameter 30 mm, to a bigger circle, of diameter 48 mm, and a cogwheel of diameter 43.5 mm with cogs of diameter 4 mm. The other control parameters are the same that the reference experiments: foam thickness of 3.5 mm, bulk viscosity of 1.06 mm^2 s^{-1} and bubble area of 16.0 mm^2. This area is suitable for bubbles to be trapped into the cogs of the cogwheel, defining an effective circular obstacle constituted by the cogwheel and the trapped bubbles, of diameter 47.5 mm, comparable to the big circle. In this paragraph, we thus study the influence of the size and of the boundary of the obstacle. These obstacles sharing the circular symmetry, we choose to study them in polar coordinates, plotting the component v_r and $-v_\theta$ of the velocity, the pressure, and the deviatoric component of the statistical elastic strain tensor $U_{rr} - U_{\theta\theta}$, as functions of θ along a circle located at 1.5 cm from the obstacle boundary (Fig. 25).

The data for the big circle and the cogwheel are very similar, showing that the boundary conditions have little influence on the behavior of the foam. The comparison between the two circles show that whereas the radial component of the velocity is almost equal, the amplitude of the orthoradial component is bigger for the bigger circle. This is actually a consequence of the constriction between the obstacles and the channel walls: more precisely, at the angle $\theta = 90°$, we have $-v_\theta/v_0 = v_y/v_0 = 1.83$ for the circle of diameter 48 mm, and $-v_\theta/v_0 = 1.41$ for the circle of diameter 30 mm, which is comparable to the aspect ratio $h/(h-D)$, with $h = 10$ cm the channel width and D the obstacle diameter: this ratio equals 1.92 and 1.43 for these two circles. Moreover, whereas the amplitude of variation of the pressure is weaker for the small circle, the statistical elastic strain component $U_{rr} - U_{\theta\theta}$ does not change much between the three obstacles. It is negative and almost constant for angles between 100 and 180° (Fig. 25), which corresponds actually to an extended region where the yield strain is reached; the component $U_{rr} - U_{\theta\theta}$ has a markedly different behavior for angles between 0 and 100°, where it follows a monotonic, almost linear evolution, which is the signature of an elastic-like transition to another yielded region, situated in the wake of the obstacle. This is confirmed by the polar dependence of the frequency of T1s (Fig. 20), which shows a high frequency in the yielded regions for angles close to 0° and comprised between 100 and 180°, whereas the frequency of T1s is lower in between. A simple sketch of this behavior, with a yielded region on the whole leading side of the obstacle and an elastic
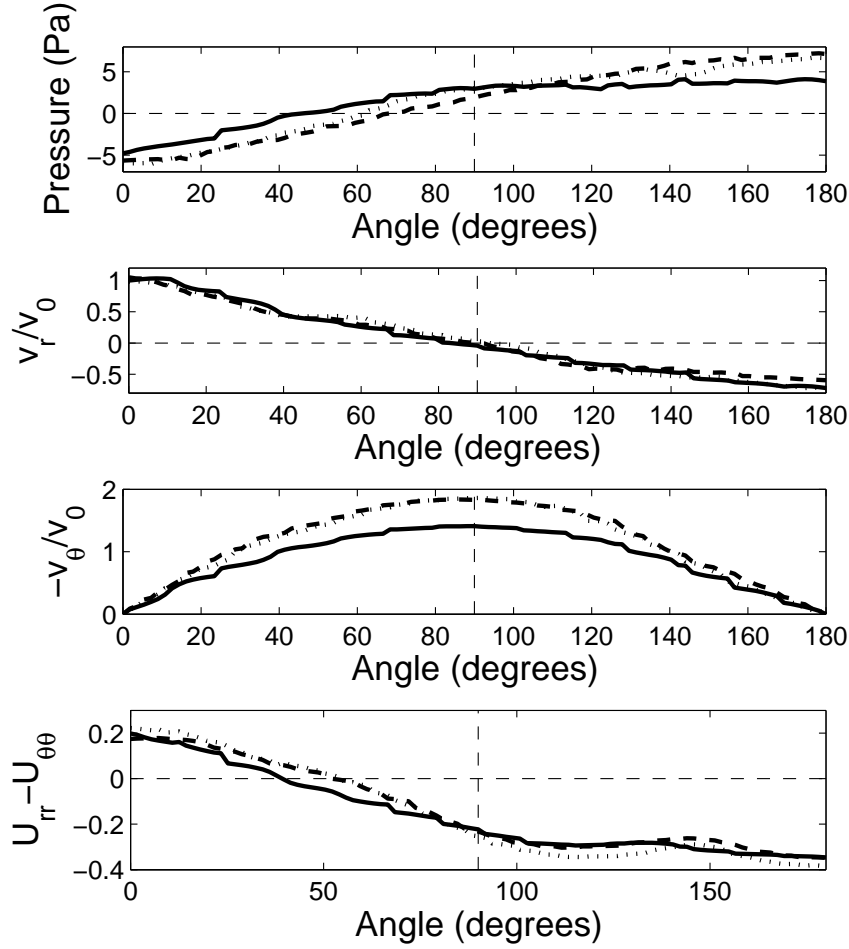
FIG. 25: From top to bottom: plot of the pressure, of the components v_r/v_0 and $-v_\theta/v_0$ of the dimensionless velocity, and of the component $U_{rr}-U_{\theta\theta}$ of the statistical elastic strain, for the circles of diameter 30 mm (plain line) and 48 mm (long-dashed line), and the cogwheel (short-dashed line) as a function of the angle θ, between 0 and 180°. The flow being symmetric with respect to the axis $y=0$, the data have been averaged with the angles between -180 and 0°.

transition at the trailing side to another yielded region in the wake, helps to understand the fluid fraction dependence of the drag on circles ([42]) as well as the angular dependence of the drag, lift and torque experienced by an ellipse ([19]).

IV. DISCUSSION

A. Liquid foam: localization or continuity?

Our analysis of Section III A, showing that the fluctuations are like a white noise, suggests that the foam behaves as a continuous medium. We do not measure large-scale correlations of plastic rearrangements. This is to compare to flows involving pure shear, like experiments in Couette geometry ([13, 33, 39]). In this case, a disordered and wet foam in a Hele-Shaw cell exhibits a strong discontinuity in the form of a localised shear band ([13]), resulting from large-scale avalanches of T1 ([25]), but a disordered and wet bubble raft shows no such bands ([34]). This suggests that the friction between the foam and the boundaries alters the continuity of any quasi-2D foam. Indeed, a recent study has shown that at given flow rate in the same Couette geometry, liquid pool foams exhibit localization contrary to bubble rafts ([49]).

However, our liquid pool foam does not exhibit localisation. Actually, the flow around an obstacle is more complex than a pure shear and screens the correlations of T1s, even though we have very ordered foams. Qualitatively, we only saw large-scale correlations with very wet and ordered foams, where dislocations between rows of bubbles can occur on distances of several centimeters. In the experiments presented here, it only occurs for the smallest foam thickness.

B. Discussion of the reference experiment

1. Velocity

A salient feature of the flow of foam around an obstacle is the asymmetry up/downstream of the velocity field. Such an asymmetry is not captured by the models of Bingham plastics ([37, 43]) or Herschel-Bulkley fluids ([4]) usually invoked to simply model liquid foams. It is an elastic effect, and the velocity overshoot in the wake of the obstacle (Fig. 9) has already been reported (and termed negative wake) for a number of other elastic fluids (see e.g. [20, 29]). However, a more quantitative comparison to other viscoelastic fluids is difficult, because of the boundary conditions: for a viscoelastic fluid, there is no slip against a solid boundary, whereas at the macroscopic scale, the foam slips against the walls and the

obstacle (Fig. 8). More precisely, a high velocity gradient is concentrated in the thin liquid film between the solid boundaries and the neighboring bubbles.

2. Pressure

We showed that the pressure in maximal at the upstream side of the obstacle, and minimal at the downstream side (Section III B 2), and that it does not depend significantly on the flow rate (Section III C 1). This suggests that the pressure is mainly of elastic origin, which is also corroborated by the anti-inertial lift observed for an airfoil ([18]). More precisely, fitting the data for the pressure along the axis $y = 0$ (Fig. 21) by a power-law yields the following dependence: $P(x) = (9.5 \pm 0.7)x^{-1.13 \pm 0.05}$ (expressed in Pa). The exponent is close to -1, which is coherent with the stress distribution is an elastic medium under a point-like force ([30]).

3. Coupling between statistical elastic strain, velocity gradients and T1s

The asymmetric repartition of the T1s (Fig. 19) is a major result of this study, since the plastic flow of the foam results from the superposition of many T1s. Since T1s more likely occur for deformed bubbles, it is interesting to compare their repartition with the map of statistical elastic strain (Fig. 12). Such a comparison reveals that the regions of frequent T1s indeed correspond to high deformation, but the correlation is not so simple: for instance, upstream from the obstacle, the deformation is maximal at $x = 0$ (Fig. 13), whereas the T1s occur more likely on the sides of the obstacle, not at $x = 0$ (Fig. 20). This occurs because in this region, the velocity gradients acts to increase the preexistent deformation (Fig. 14). There is thus a strong coupling between the statistical elastic strain, the velocity gradients and the T1 repartition, which is analysed in more detail elsewhere ([Marmottant *et al.*]).

C. Influence of the control parameters and comparison with force measurements

We now compare qualitatively our results to the force measurements realized in the same conditions in [16]. To summarize, this study showed that the drag exerted by a flowing foam

on a circular obstacle scales as:

$$F = F_0 + \text{cste} \times \eta^{0.77} v_0, \tag{4}$$

with η the bulk viscosity, and F_0 a decreasing function of the bubble area. The independence of the pressure and the bubble deformation on the flow rate is in qualitative agreement with the linear increase of the force exerted by the flowing foam on the obstacle ([16]), if we assume that the velocity-dependent contribution to the force is mainly due to the viscous friction in the liquid films between the obstacle and the surrounding bubbles. Moreover, the exponent for the bulk viscosity in (4) is close to 1, which is compatible with the weak influence of this parameter (Fig. 24). Concerning the foam thickness, Fig. 23 shows that the up/downstream differences increases with the foam thickness, hence decreases with the fluid fraction. This is compatible with the decrease of the drag with the fluid fraction reported in [42]. The role of the bubble area is more complex: we showed in Section III C 2 that this parameter does not influence much the bubble deformation, but that the up/downstream difference in pressure decreases with increasing bubble area. The bubble deformation and pressure being the two contributions to the yield drag F_0 in (4), this qualitatively agrees with the fact that F_0 decreases with the bubble area. However, we do not understand yet why the behavior of the pressure and deformation differs so markedly. The last studied control parameter, the obstacle itself, shows that the boundary conditions at the obstacle plays no significant role. The size of the obstacle has two influences: the bigger the circle, the higher the velocity at its sides, due to the imposed constriction, and the higher the amplitude of variation of the pressure. This is compatible with the measured values of the drag coefficient (ratio of drag and obstacle radius) reported in [16] for these three obstacles, equal for the cogwheel and the big circle, and slightly lower for the small circle.

V.   CONCLUSIONS

We performed a systematic local description of the flow of foam around a circular obstacles, quantifying the elasticity by the statistical elastic strain tensor and the pressure field, the plasticity by a tensorial descriptor of bubble rearrangements, and the flow by the velocity field and its gradients. We demonstrate in Section III A that such a continuous approach is justified and suitable in this case. The study of a reference experiment (Section III B) shows

a marked asymmetry up/downstream: the velocity exhibits an overshoot in the wake, and the bubble rearrangements spread more at the leading side than in the wake of the obstacle. This reveals the complex behavior of the foam, dictated by the coupling between elasticity (bubble deformations), plasticity (bubble rearrangements) and flow (velocity gradients).

We showed in Section III C 1 that the rescaled velocity $\vec{v}/v_0$, the pressure and the bubble deformation do not depend significantly on the flow rate, in the studied range. Hence, the yield and the dynamic contributions in foam rheology seem to be decoupled, which justifies recent approaches to model foam flows (and more generally, complex fluid flows) as Bingham plastics with an added elastic term independent of the shear rate ([47, 51]). However, such scalar approaches are not sufficient in our context, where the complex flow around an obstacle appeals for a tensorial description. It would be interesting to perform the same experiments at higher flow rate, to determine when this decoupling between elastic and dynamic contribution breaks down, and to investigate whether phenomena such as elastic turbulence ([21]) could then occur in the wake of the obstacle.

The detailed results shown in Section III, combined with the associated force measurements reported in [16], severely constrain the rheological models adapted to describe liquid foams. The foam flowing around an obstacle intrinsically exhibits yield stress and dissipation (yield drag on the obstacle ([12, 16])), and elastic stress (up/downstream asymmetry); all these effects can only be captured by a whole elastoviscoplatic model.

---

[1] M. Asipauskas, M. Aubouy, J. A. Glazier, F. Graner & Y. Jiang 2003 A texture tensor to quantify deformations: The example of two-dimensional flowing foams. *Granular Matt.* **5**, 71–74.

[2] M. Aubouy, Y. Jiang, J. A. Glazier & F. Graner 2003 A texture tensor to quantify deformations. *Granular Matt.* **5**, 67–70.

[3] G. K. Batchelor 1970 The stress system in a suspension of force-free particles. *J. Fluid Mech.* **41**, 545–570.

[4] M. Beaulne & E. Mitsoulis 1997 Creeping motion of a sphere in tubes filled with Herschel–Bulkley fluids *J. Non-Newtonian Fluid Mech.* **72**, 55–71.

[5] I. Cantat & R. Delannay 2003 Dynamical transition induced by large bubbles in two-

dimensional foam flows. *Phys. Rev. E* **67**, 031501.

[6] I. CANTAT, N. KERN & R. DELANNAY 2004 Dissipation in foam flowing through narrow channels. *Europhys. Lett.* **65**, 726–732.

[7] I. CANTAT & R. DELANNAY 2005 Dissipative flows of 2D foam. *Eur. Phys. J. E* **18**, 55–67.

[8] I. CANTAT & O. PITOIS 2005 Mechanical probing of liquid foam ageing. *J. Phys. Condens. Matt.* **17**, S3455–S3461.

[9] S. COURTY, B. DOLLET, F. ELIAS, P. HEINIG & F. GRANER 2003 Two-dimensional shear modulus of a Langmuir foam. *Europhys. Lett.* **64**, 709–715.

[10] S. J. COX, M. D. ALONSO, S. HUTZLER, D. WEAIRE 2000 The Stokes experiment in a foam, in *Proceedings of the 3rd Euroconference on Foams, Emulsions and their Applications*, P. L. J. Zitha, J. Banhard, P. L. M. M. Verbist Eds., MIT Verlag, Bremen, 282–289 (2000).

[11] S. COX, M. F. VAZ & D. WEAIRE 2003. *Euro. Phys. J. E* **11**, 29–35.

[12] J. R. DE BRUYN 2004 Transient and steady-state drag in foam. *Rheol. Acta* **44**, 150–159.

[13] G. DEBRÉGEAS, H. TABUTEAU & J.-M. DI MEGLIO 2001 Deformation and flow of a two-dimensional foam under continuous shear. *Phys. Rev. Lett.* **87**, 178305.

[14] N. D. DENKOV, V. SUBRAMANIAN, D. GUROVICH & A. LIPS 2005 Wall slip and viscous dissipation in sheared foams: Effect of surface mobility. *Coll. Surf. A* **263**, 129–145.

[15] B. DERJAGUIN 1933 Die elastischen Eigenschaften der Schäume. *Kolloid Z.* **64**, 1–6.

[16] B. DOLLET, F. ELIAS, C. QUILLIET, C. RAUFASTE, M. AUBOUY & F. GRANER 2005a Two-dimensional flow of foam around an obstacle: Force measurements. *Phys. Rev. E* **71**, 031403.

[17] B. DOLLET, F. ELIAS, C. QUILLIET, A. HUILLIER, M. AUBOUY & F. GRANER 2005b Two-dimensional flows of foam: Drag exerted on circular obstacles and dissipation. *Colloids Surf. A* **263**, 101–110.

[18] B. DOLLET, M. AUBOUY & F. GRANER 2005 Anti-inertial lift in foams: A signature of the elasticity of complex fluids. *Phys. Rev. Lett.* **95**, 168303.

[19] B. DOLLET, M. DURTH & F. GRANER 2006 Flow of foam past an elliptical obstacle, to appear in *Phys. Rev. E*, `arXiv:cond-mat/0601100`.

[20] H. S. DOU & N. PHAN-THIEN 2003 Negative wake in the uniform flow past a cylinder. *Rheol. Acta* **42**, 383–409.

[21] A. GROISMAN & V. STEINBERG 2000 Elastic turbulence in a polymer solution flow *Nature*

405, 53–55.

[22] É. Guyon, J.-P. Hulin & L. Petit 2001 *Hydrodynamique physique*, EDP Sciences/CNRS Éditions, Paris.

[23] R. Höhler & S. Cohen-Addad 2005 Rheology of liquid foams *J. Phys. Condens. Matter* **17**, R1041–R1069.

[24] É. Janiaud & F. Graner 2005 Foam in a two-dimensional Couette shear: A local measurement of bubble deformation. *J. Fluid Mech.* **532**, 243–267.

[25] A. Kabla & G. Debrégeas 2003 Local stress relaxation and shear-banding in a dry foam under shear. *Phys. Rev. Lett.* **90**, 258303.

[26] N. Kern, D. Weaire, A. Martin, S. Hutzler & S. J. Cox 2004 Two-dimensional viscous froth model for foam dynamics, *Phys. Rev. E* **70**, 041411.

[27] S. A. Khan & R. C. Armstrong 1986 Rheology of foams. I. Theory for dry foams. *J. Non-Newtonian Fluid Mech.* **22**, 1–22.

[28] S. A. Khan & R. Prud'homme 1996 *Foams*, Dekker, New York.

[29] J. M. Kim, C. Kim, C. Chung, K. H. Ahn & S. J. Lee 2005 Negative wake generation of FENE–CR fluids in uniform and Poiseuille flow past a cylinder. *Rheol. Acta* **44**, 600–613.

[30] L. D. Landau & E. M. Lifshitz 1986 *Theory of elasticity*, 3rd edition, Reed, Oxford.

[31] S. A. Langer & A. J. Liu 1997 Effect of random packing on stress relaxation in foam. *J. Phys. Chem. B* **101**, 8667–8671.

[32] R. G. Larson 1999 *The structure and rheology of complex fluids*, Oxford University Press, New York.

[33] J. Lauridsen, M. Twardos & M. Dennin 2002 Shear-induced stress relaxation in a two-dimensional wet foam. *Phys. Rev. Lett.* **89**, 098303.

[34] J. Lauridsen, G. Chanan & M. Dennin 2004 *Phys. Rev. Lett.* Velocity profiles in slowly sheared bubble rafts **93**, 018303.

[Marmottant *et al.*] P. Marmottant, B. Dollet, C. Raufaste & F. Graner Observation and prediction of local rearrangements: Plasticity in a flowing foam, submitted.

[35] T. G. Mason, J. Bibette & D. A. Weitz 1995 Elasticity of compressed emulsions. *Phys. Rev. Lett.* **75**, 2051–2054.

[36] T. G. Mason, J. Bibette & D. A. Weitz 1996 Yielding and flow of monodisperse emulsions. *J. Coll. Int. Sci.* **179**, 439–448.

[37] E. MITSOULIS 2004 On creeping drag flow of a viscoplatic fluid past a circular cylinder: Wall effects. *Chem. Eng. Sci.* **59**, 789–800.

[38] G. PICARD, A. ADJARI, F. LEQUEUX & L. BOCQUET 2004 Elastic consequences of a single plastic event: A step towards the microscopic modeling of the flow of yield stress fluid. *Eur. Phys. J. E* **15**, 371–381.

[39] E. PRATT & M. DENNIN 2003 Nonlinear stress and fluctuation dynamics of sheared disordered wet foam *Phys. Rev. E* **67**, 054102.

[40] H. M. PRINCEN 1983 Rheology of foams and highly concentrated emulsions. I. Elastic properties and yield stress of a cylindrical model system. *J. Coll. Int. Sci.* **91**, 160–175.

[41] H. M. PRINCEN 1985 Rheology of foams and highly concentrated emulsions. II. Experimental study of the yield stress and wall effects for concentrated oil-in-water emulsions. *J. Coll. Int. Sci.* **105**, 150–171.

[42] C. RAUFASTE, B. DOLLET, S. COX, F. GRANER & Y. JIANG Yield drag in a two-dimensional foam around a circular obstacle: Effect of fluid fraction, in preparation.

[43] N. ROQUET & P. SARAMITO 2003 An adaptive finite element mathod for Bingham fluid flows around a cylinder *Comput. Methods Appl. Mech. Eng.* **192**, 3317–3341.

[44] A. SAINT-JALMES & D. J. DURIAN 1999 Vanishing elasticity for wet foams: Equivalence with emulsions and role of polydispersity. *J. Rheol.* **43**, 1411–1422.

[45] P. SOLLICH, F. LEQUEUX, P. HÉBRAUD & M. E. CATES 1997 Rheology of soft glassy materials. *Phys. Rev. Lett.* **78**, 2020–2023.

[46] D. STAMENOVIĆ & T. A. WILSON 1984 The shear modulus of liquid foam. *J. Appl. Mech.* **51**, 229–231.

[47] O. TAKESHI & K. SEKIMOTO 2005 Internal stress in a model elastoplastic fluid. *Phys. Rev. Lett.* **95**, 108301.

[48] M. F. VAZ & S. J. COX 2005 Two-bubble instabilities in quasi-two-dimensional foams. *Phil. Mag. Lett.* **85**, 415–425.

[49] Y. WANG, K. KRISHAN & M. DENNIN 2006 Impact of boundaries on velocity profiles in bubble rafts. *Phys. Rev. E* **73**, 031401.

[50] D. WEAIRE & S. HUTZLER 1999 *The Physics of Foams*, Oxford University Press, Oxford.

[51] D. WEAIRE, É. JANIAUD & S. HUTZLER Two-dimensional foam rheology with viscous drag, submitted, `arXiv:cond-mat/0602021`.